

# STIS Longslit Spectroscopy of the Narrow-Line Region of NGC 4151.

## II. Physical Conditions along Position Angle 221<sup>o1</sup>

S. B. Kraemer<sup>2</sup>, D. M. Crenshaw<sup>2</sup>, J. B. Hutchings<sup>3</sup>, T. R. Gull<sup>4</sup>, M. E. Kaiser<sup>5</sup>, C. H.  
Nelson<sup>6</sup>, & D. Weistrop<sup>6</sup>

Received \_\_\_\_\_; accepted \_\_\_\_\_

---

<sup>1</sup>Based on observations made with the NASA/ESA Hubble Space Telescope. STScI is operated by the Association of Universities for Research in Astronomy, Inc. under the NASA contract NAS5-26555.

<sup>2</sup>Catholic University of America, NASA/Goddard Space Flight Center, Code 681, Greenbelt, MD 20771; stiskraemer@yancey.gsfc.nasa.gov, crenshaw@buckeye.gsfc.nasa.gov.

<sup>3</sup>Dominion Astrophysical Observatory, National Research Council of Canada, 5071 W. Saanich Rd., Victoria, B.C. V8X 4M6, Canada, John.Hutchings@hia.nrc.ca

<sup>4</sup>NASA's Goddard Space Flight Center, Laboratory for Astronomy and Solar Physics, Code 681, Greenbelt, MD 20771, gull@sea.gsfc.nasa.gov

<sup>5</sup>Department of Physics and Astronomy, Johns Hopkins University, Baltimore, MD 21218, kaiser@munin.pha.jhu.edu

<sup>6</sup>Department of Physics, University of Nevada, Las Vegas, 4505 Maryland Parkway, Las Vegas, NV 89154-4002, cnelson@physics.unlv.edu, weistrop@nevada.edu

## ABSTRACT

We have examined the physical conditions in the narrow-line region of the well-studied Seyfert galaxy NGC 4151, using long-slit spectra obtained with the *Hubble Space Telescope*/Space Telescope Imaging Spectrograph (*HST*/STIS). The data were taken along a position angle of  $221^\circ$ , centered on the optical nucleus. We have generated photoionization models for a contiguous set of radial zones, out to  $2''.3$  in projected position to the southwest of the nucleus, and  $2''.7$  to the northeast. Given the uncertainties in the reddening correction, the calculated line ratios successfully matched nearly all the dereddened ratios. We find that the narrow-line region consists of dusty atomic gas photoionized by a power-law continuum that has been modified by transmission through a mix of low and high ionization gas, specifically UV and X-ray absorbing components. The physical characteristics of the absorbers resemble those observed along our line of sight to the nucleus, although the column density of the X-ray absorber is a factor of ten less than observed. The large inferred covering factor of the absorbing gas is in agreement with the results of our previous study of UV absorption in Seyfert 1 galaxies. We find evidence, specifically the suppression of  $L\alpha$ , that we are observing the back-end of dusty ionized clouds in the region southwest of the nucleus. Since these clouds are blueshifted, this supports the interpretation of the cloud kinematics as being due to radial outflow from the nucleus. We find that the narrow-line gas at each radial position is inhomogeneous, and can be modeled as consisting of a radiation-bounded component and a more tenuous, matter-bounded component. The density of the narrow-line gas drops with increasing radial distance, which confirms our earlier results, and may be due to the expansion of radially outflowing emission-line clouds.

*Subject headings:* galaxies: individual (NGC 4151) – galaxies: Seyfert

## 1. Introduction

NGC 4151 is one of the nearest ( $z=0.0033$ ) Seyfert galaxies, and among the most extensively studied. Based on its strong broad (FWHM  $\sim 5000$  km s $^{-1}$ ) permitted lines and our direct line of sight to the non-thermal continuum source, NGC 4151 is generally classified as a Seyfert 1 galaxy, although its continuum and broad emission lines are extremely variable and at one time the broad component nearly disappeared (Penston and Perez 1984), at which time the spectrum of NGC 4151 resembled that of a Seyfert 2 galaxy. It has an extended emission-line region (i.e. narrow-line region, NLR) which is often cited as an example of the biconical morphology resulting from collimation of the ionizing radiation (cf. Schmitt & Kinney 1996). A linear radio structure (“jet”) extends  $3''.5$  southwest of the nucleus (Wilson & Ulvestad 1982) and may be the result of the interaction of radially accelerated energetic particles with the interstellar magnetic field of NGC 4151. There have been suggestions, most recently by Wilson & Raymond (1999), that the interaction of the jet with interstellar gas could be the source of the narrow-line emission. Much of the gas in the NLR appears to be radially outflowing from the nucleus (Hutchings et al. 1998), although there is no apparent correlation of the kinematics of the emission-line gas and the radio structure (Kaiser et al. 1999), which suggests another source for the radial outflow, such as a wind emanating from the inner regions of the nucleus (cf. Krolik & Begelman 1984).

One of the most interesting spectral characteristics of NGC 4151 is the presence of absorption by atomic gas, seen in the UV (cf. Weymann et al. 1997) and X-ray (cf. Holt et al. 1980). The variability of the absorption features suggest that the absorbing material must lie close to the nucleus, within the inner few parsecs for the UV absorber (Espey et al. 1998) and within a parsec for the X-ray absorber (Yaqoob, Warwick, & Pounds 1989). Although the absorbers can only be detected along our line of sight to the nucleus, their

effect on the gas further out should be apparent (Kraemer et al. 1999) if they have a large covering factor, as suggested by Crenshaw et al. (1999). In fact, Alexander et al. (1999) have demonstrated that narrow emission lines of NGC 4151 could be the result of photoionization by an absorbed continuum. However, the heterogeneous nature of their data, and the lack of spatially resolved spectra, prevented them from constraining the spectral energy distribution (SED) of the ionizing continuum, other than by noting the apparent paucity of photons just above the He II Lyman limit (54.4 eV).

We have obtained low-dispersion long-slit data, at a position angle  $PA = 221^\circ$ , using *HST*/STIS. From these data, coupled with detailed photoionization models, we are able to determine the physical conditions of the NLR gas, including any radial variations. As we will show in the following sections, there is no evidence at this position angle for other sources of ionization other than photoionization by the nuclear continuum. The NLR does indeed appear to be ionized by an absorbed continuum, as proposed by Alexander et al. (1999). Furthermore, based on our modeling, we can place much tighter constraints on the SED of the ionizing radiation. Finally, these data provide further evidence that the NLR gas is outflowing radially from the nucleus of NGC 4151.

## 2. Observations and Analysis

The details of the observations and data reduction are described in Nelson et al. (1999, hereafter Paper I). To summarize, we used the G140L grating with the far-UV MAMA detector and the G230LB, G430L, and G750L gratings with the CCD detector, to cover the entire  $1150 - 10,270 \text{ \AA}$  region, at a resolving power of  $\lambda/\Delta\lambda = 500 - 1000$ . We used a narrow slit width of  $0''.1$  to avoid degradation of the spectral resolution. We extracted fluxes in bins with lengths of  $0''.2$  in the inner  $1''$  and  $0''.4$  further out to maximize the signal-to-noise ratios of the He II lines (see below) and yet isolate the emission-line knots

identified in our earlier paper (Hutchings et al. 1998).

Our measurement techniques follow those used in previous papers (cf., Kraemer, Ruiz, & Crenshaw 1998). We obtained fluxes for nearly all of the emission lines by direct integration over a local baseline (see Paper I). For the blended lines of  $H\alpha$  and  $[N\ II]\ \lambda\lambda 6548, 6584$ , and  $[S\ II]\ \lambda\lambda 6716, 6731$ , we used the  $[O\ III]\ \lambda 5007$  line as a template. We determined the reddening from the observed  $He\ II\ \lambda 1640/\lambda 4686$  ratios, assuming an intrinsic ratio of 7.2 (expected from NLR temperatures and densities), and the Galactic reddening curve of Savage & Mathis (1979). We determined the errors in the observed ratios (relative to  $H\beta$ ) from the sum in quadrature of photon noise and different reasonable continuum placements. Errors in the dereddened ratios include an additional contribution (added in quadrature) from the uncertainty in reddening (propagated from errors in the  $He\ II$  ratios); the latter dominates the errors in the dereddened UV lines.

Tables 1 and 2 give the dereddened ratios and errors in each bin, along with the reddening and its uncertainty, and the total  $H\beta$  flux in that bin (the observed ratios are included in Paper I). For positions that include a knot of emission that we identified in an earlier paper (Hutchings et al. 1998), we list that knot. We note that the sensitivity of the G230LB grating is very low at the short wavelength end, and thus we could not detect the  $[N\ III]\ \lambda 1750$  line. The errors in the lines longward of  $7000\ \text{\AA}$  are probably underestimates since this region of the G750L spectrum suffers from fringing (Plait & Bohlin 1998).

### 3. General Trends in the Line Ratios

Figure 1 shows various trends in the reddening and line ratios as a function of projected distance along the slit. The central position of each bin is plotted along the horizontal axis, with the convention that negative numbers represent the blueshifted (southwest) side.

From the first plot, we see that there is significant reddening at many positions, whereas a few positions have essentially no reddening. The reddening does not appear to vary in a uniform fashion over this region, which suggests that it is not due to an external screen, but is associated with the emission-line knots. If we look at the inner region ( $\pm 1''$ ), where the errors are smaller, there *may* be a trend, in that the reddening seems to drop from blueshifted to redshifted side.

The dereddened  $L\alpha/H\beta$  plot shows a very interesting trend: this ratio increases dramatically from the blueshifted to redshifted side. Since there is no correlation between the reddening and the  $L\alpha/H\beta$  ratio, this trend cannot be explained by a systematic error in determining the reddening. In the inner region, higher values of reddening on the redshifted side (see the previous plot), would only make the  $L\alpha/H\beta$  trend steeper.

The  $L\alpha/H\beta$  trend can be explained by radial outflow of optically thick clouds that contain dust. In such a cloud, resonance-line photons (and  $L\alpha$  in particular) are selectively destroyed by multiple scatterings and eventual absorption by dust (cf. Cohen, Harrington, & Hess 1984). The observer sees a much higher  $L\alpha/H\beta$  ratio when looking at the illuminated face of a cloud (as opposed to the back side), since escape of the  $L\alpha$  photons is much easier in this direction. Thus, we expect higher  $L\alpha/H\beta$  ratios for clouds on the far side of the nucleus, which in this case corresponds to redshifted clouds, indicating radial outflow (see Capriotti, Foltz, & Byard 1979). Although the UV absorption lines are blue-shifted (Weymann et al. 1997), indicating that components of gas in our line-of-sight are outflowing, the suppression of  $L\alpha$  is the strongest evidence that the emission line gas in the inner NLR of NGC 4151 is outflowing radially (for further discussion of the NLR kinematics, see Hutchings et al. 1998; Kaiser et al. 1999; Paper I).

The  $[O III]/H\beta$  plot verifies a trend that we first observed in our slitless data (Kaiser et al. 1999). In the inner NLR, this ratio decreases with increasing projected distance

from the nucleus. Since the ionization parameter is proportional to  $n_H^{-1}r^{-2}$ , (where  $n_H$  is the atomic hydrogen density and  $r$  is the distance from the nucleus), we suggested that  $n_H$  decreases roughly as  $r^{-1}$  in the inner NLR, and more steeply with increasing distance (Kaiser et al. 1999). However, we will show in the discussion of the model results that the closest radial points are best fit by assuming a nearly constant ionization parameter, which indicates that  $n_H$  decreases more as  $r^{-1.6}$  to  $-1.7$ .

In the last plot, we show the  $H\gamma/H\beta$  ratio as a function of projected distance. The ratio of these H recombination lines should show no trend, since it only has a slight dependence on temperature and density. In fact, we see that there is no observed trend, and are therefore confident that there are no large systematic errors in the ratios.

#### 4. Photoionization Models

The basic methodology which we employ and the details of our photoionization code have been described in our previous publications (cf. Kraemer 1985; Kraemer et al. 1994). The models assume plane-parallel geometry and emission-line photon escape out either the illuminated face or the back-end of the slab. In the latter case, the back surface of the slab was assumed to be the point where the model was truncated (that is we ignored any effect from an additional neutral envelope). In practice, we used the back-end values for the three positions with a dereddened  $L\alpha/H\beta < 5$ . Most of the other line ratios are not affected by the choice of front- or back-end escape, due to the low column densities for these models (see Section 5.1).

The photoionization models are parameterized in terms of the density of atomic hydrogen ( $n_H$ ) and the dimensionless ionization parameter at the illuminated face of a cloud:



$$U = \frac{1}{4\pi D^2 n_H c} \int_{\nu_0}^{\infty} \frac{L_\nu}{h\nu} d\nu, \quad (1)$$

where  $L_\nu$  is the frequency dependent luminosity of the ionizing continuum,  $D$  is the distance between the cloud and the ionizing source and  $h\nu_0 = 13.6$  eV.

#### 4.1. The Ionizing Continuum

We have assumed in these simple models that the gas is photoionized by radiation from the central AGN. As has often been demonstrated (cf., Binette, Robinson, & Courvoisier 1988), the physical conditions in the NLR, and, hence, resulting emission-line spectrum, depend on both the intensity of the radiation field and its SED. Along our line-of-sight, the continuum radiation from NGC 4151 shows the effects of a complex system of absorbers, which is interior to the NLR and can alter the SED that the NLR sees drastically. Kraemer et al. (1999) have demonstrated that, for typical NLR conditions ( $U = 10^{-2.5}$ ,  $n_H \leq 10^5$  cm $^{-3}$ ), the ratio of [O III]  $\lambda 4363$  to He II  $\lambda 4686$  increases as the depth of the absorption near the He II Lyman edge increases. From the observed ratios of these lines (see Tables 1 and 2), it is clear that [O III]  $\lambda 4363$  is relatively strong. Therefore, our approach was to estimate the intrinsic (unabsorbed) SED as simply as possible, and then include the effects of absorption to replicate the ionization state and electron temperature of the NLR gas. We constrained the physical characteristics of the absorbers to resemble those observed along our line-of-sight. The SED was then held fixed as an input to the models. Although Alexander et al. (1999) determined the general characteristics of the SED from emission-line diagnostics, they did not attempt to model the affects of realistic absorbers.

In order to approximate the intrinsic SED, we used the observed fluxes at energies where the effects of the absorber are not severe, specifically at energies lower than the Lyman limit and above several keV. In the 1 – 4 keV band, the continuum radiation

from NGC 4151 has been modified by a large absorbing column of gas (Barr et al. 1977; Mushotzky, Holt, & Serlemitsos 1978), which may have multiple components (Weaver et al. 1994). For the purposes of these models, we assumed that the absorption at 5 keV is negligible and that the X-ray continuum down to 1 keV can be approximated by a power-law ( $F_\nu \propto \nu^{-\alpha}$ ) with spectral index,  $\alpha \approx 0.5$  (Weaver et al. 1994). For the 5 keV flux, we have used the value from *ASCA* observations given in Edelson et al. (1996).

The far-UV continuum of NGC 4151 has been observed by HUT on both Astro-1 (Kriss et al. 1992) and Astro-2 (Kriss et al. 1995) missions and with the Berkeley spectrometer during the ORFEUS-SPAS II mission (Espey et al. 1998). Between the two HUT observations, the continuum flux at 1455 Å increased by a factor of  $\sim 5$  (Kriss et al. 1995), and somewhat more near the Lyman limit (the ORFEUS results are similar to those from Astro-2). Note, however, that the continuum irradiating any parcel of NLR gas is time averaged over the light crossing time to that parcel. Thus, variations in the nuclear continuum flux on time scales of a few years will be insignificant, since our measurements are sampling at least 30 years of continuum variations. To be conservative, we assumed a reddening corrected flux at the Lyman limit that is the average of the two HUT values.

As noted above, the X-ray continuum can be approximated by a hard power-law, the extrapolation of which would lie far below the observed flux near the Lyman limit. Since many Seyfert spectra appear to steepen in the soft X-ray (cf., Arnaud et al. 1985; Turner et al. 1999), we assume that the X-ray continuum of NGC 4151 extends to 1 keV, where the index becomes steeper, continuing down to the Lyman limit, and flattens to the canonical value ( $\alpha = 1$ ) below 13.6 eV. The ionizing continuum is thus expressed as  $F_\nu = K\nu^{-\alpha}$ , where

$$\alpha = 1.0, \quad h\nu < 13.6 \text{ eV} \tag{2}$$

$$\alpha = 1.4, \quad 13.6 \text{ eV} \leq h\nu < 1000 \text{ eV} \tag{3}$$

$$\alpha = 0.5, h\nu \geq 1000 \text{ eV} \quad (4)$$

The total luminosity between 13.6 eV and 1 KeV is  $\approx 1.2 \times 10^{43} \text{ erg s}^{-1}$ . Although based on their models of the extended ( $\geq 500 \text{ pc}$ ) emission-line region, Schulz & Komossa (1993) have argued for the existence of a “Big Blue Bump” in the EUV continuum of NGC 4151, Alexander et al. (1999) have demonstrated that the NLR shows no such effects. Furthermore, as we will show, this simple power-law fit provides a sufficient flux in ionizing radiation to power the NLR, even after including the effects of absorption near the He II Lyman limit. Hence, there is no reason to include a blue bump.

There have been several attempts to constrain the physical properties of the X-ray absorber using photoionization models (Yaqoob, Warwick, & Pounds 1989; Weaver et al. 1994; Warwick, Done, & Smith 1995) and, while it is likely to consist of multiple components, there is general agreement that  $U$  is in the range 0.2-1.1, with column density,  $N_H \sim 10^{23} \text{ cm}^{-2}$ , where  $N_H$  is the sum of both ionized and neutral hydrogen. One effect of the X-ray absorber is to produce deep O VII and O VIII absorption edges (739 eV and 871 eV, respectively). Absorption of continuum photons at these energies results in a lower electron temperature in the NLR gas, particularly in the partially ionized, X-ray heated envelope behind the  $H^+/H^0$  transition zone. In addition to the large column of X-ray absorbing material, there is a component of lower column, lower ionization gas, which is the source of the UV resonance line absorption which has been observed with *IUE* (Bromage et al. 1985) and *HST* (Weyman et al. 1997). Kriss (1998) has modeled several different kinematic components of the UV absorber with  $N_H \sim 10^{19.5} \text{ cm}^{-2}$  and  $U \geq 10^{-3.0}$ . Such an absorber is optically thick at the He II Lyman limit and would produce the effects on emission-line diagnostics discussed in Kraemer et al. (1999).

For our models, we used a single X-ray absorber and a single UV absorber along each of the two lines-of-sight (SW and NE). For the X-ray absorber we obtained the best fit

to the average NLR conditions by assuming  $U = 1.0$  and  $N_H = 3.2 \times 10^{22} \text{ cm}^{-2}$ . For the UV absorber, we used  $U = 10^{-3.0}$  and  $N_H = 2.8 \times 10^{19} \text{ cm}^{-2}$  and  $5.6 \times 10^{19} \text{ cm}^{-2}$  for the southwest (SW) and northeast (NE) sides, respectively. The different column densities were chosen to fit the differences in the relative strengths of the [O III]  $\lambda 4363$  and He II  $\lambda 4686$  lines on each side of the nucleus. The unabsorbed and transmitted SEDs are shown in Figure 2 and 3. Note that we have assumed that the UV absorber is external to the X-ray absorber, although the NLR models are not particularly sensitive to the relative locations of the absorbers.

#### 4.2. Model Input Parameters

For the sake of simplicity, we have assumed that the measured distances are the true radial distances on the NE side of the nucleus (note that we have assumed  $H_0 = 50 \text{ km s}^{-1} \text{ Mpc}^{-1}$  for this analysis, which places NGC 4151 at a distance of 20 Mpc, and thus  $1''.0$  corresponds to 100 pc; this was done so that our results could be compared more easily with previous studies of the NLR). In our model, the smaller column of the UV absorber towards the SW permits more ionizing photons to reach the NLR. Since we do not see strong evidence for higher ionization in the SW, we have scaled the distances by a factor of 1.2. Interestingly, on the SW side we are seeing some clouds which may have a larger component of velocity in our line-of-sight (Kaiser et al. 1999), which indicates a larger projection effect, and supports the scaling of observed radial distances.

Although the UV semi-forbidden emission lines from doubly ionized carbon, nitrogen, and oxygen can be used to determine the relative abundances of each element (Netzer 1997), the poor signal-to-noise quality our long-slit data between  $1650 \text{ \AA}$  and  $1800 \text{ \AA}$  make reliable measurement of the strengths of [O III]  $\lambda 1663$  and [N III]  $\lambda 1750$  impossible. However, the relative strengths of optical forbidden lines show no evidence of peculiar abundances.

Therefore, we have assumed roughly solar abundances for these models (cf. Grevesse & Anders 1989). The abundances, relative to H by number, are He=0.1, C=3.4x10<sup>-4</sup>, O=6.8x10<sup>-4</sup>, N=1.2x10<sup>-4</sup>, Ne=1.1x10<sup>-4</sup>, S=1.5x10<sup>-5</sup>, Si=3.1x10<sup>-5</sup>, Mg=3.3x10<sup>-5</sup>, and Fe=4.0x10<sup>-5</sup>. However, as we will discuss, there is evidence for enhancement of iron close to the nucleus.

As we discussed in Section 3, the L $\alpha$ /H $\beta$  ratio is strong evidence that there is cosmic dust mixed in with the emission-line gas. However, both C II]  $\lambda$ 2328 and Mg II  $\lambda$ 2800 are relatively strong lines (about equal to H $\beta$ , after correcting for reddening), which would indicate that a substantial fraction of these elements remain in gas phase. Therefore, we have assumed that the amounts of silicate and carbonate dust grains are 50% and 20% of the Galactic values, respectively, with depletions of elements onto dust grains, scaled accordingly, as per Seab & Shull (1983).

At all of the radial locations sampled, the [O II]  $\lambda$ 3727 and [S II]  $\lambda\lambda$ 6716, 6731 lines are among the strongest optical emission lines. Since the critical electron density for [O II]  $\lambda$ 3727 is  $n_e = 4.5 \times 10^3 \text{ cm}^{-2}$  (de Robertis & Osterbrock 1984), a substantial fraction of the emission-line gas must be at densities  $n_H \leq$  a few times  $10^4 \text{ cm}^{-3}$ , although some of this emission may be due to projection of low density gas at larger radial distances. The average ratio of [S II]  $\lambda$  6716/ $\lambda$ 6731 is near unity, which is consistent with these lines arising in the partially ionized envelope associated with the [O II] clouds, and, hence, where  $n_e < n_H$ .

The spectra at each radial point show emission lines from a wide range in ionization state. For example, emission from O<sup>0</sup> through O<sup>+3</sup> are detected at every location, and, in several cases, N<sup>0</sup> through N<sup>+4</sup> are seen. It is plausible that the wide range in physical conditions indicated by the emission-line spectra is the result of local density inhomogeneities in the NLR gas. To model this effect, we have assumed that the gas in which the [O II]  $\lambda$ 3727 emission arises is optically thick (radiation-bounded) and

the principal source of hydrogen recombination radiation. To this we added a second component of less dense, optically thin (matter-bounded) gas, which is the source of the high ionization lines, such as C IV  $\lambda 1550$ , [Ne V]  $\lambda\lambda 3346, 3426$ , and most of the He II emission. The idea that high excitation lines arise in a tenuous component distributed through the NLR region of NGC 4151 has been discussed by Korista & Ferland (1989), although in our models the matter-bounded component is co-located with and has the same radial dependence in physical conditions as the denser component. We determined the relative contributions of these two components by given approximately equal weight to the predicted vs. observed fits for the following line ratios: [O III]  $\lambda 5007$ /[O II]  $\lambda 3727$ , He II  $\lambda 4686$ /H $\beta$ , and C IV  $\lambda 1550$ /H $\beta$ . The first is sensitive to ionization parameter, the second to SED and the fraction of matter-bounded to radiation-bounded gas, and the last is a trace of the high-ionization component (although sensitive to the effects of dust). In one case, the red-shifted core ( $0''.1 - 0''.3$  NE), the C III]  $\lambda 1909$ /H $\beta$  ratio was included, since the spectrum suggests the presence of an additional high density component in which the oxygen lines might be collisionally suppressed. Since there are no obvious constraints on the size of the matter-bounded component, other than the extraction length along the slit, we truncated the model such that its physical extent was approximately 10 times that of its radiation-bounded companion. We have not considered the case where the high density gas is embedded within the low density gas, although this is certainly possible. Thus, in our models, each component sees the ionizing source directly.

The input parameters for the models are given in Table 3. As noted above, the density of the dominant (radiation-bounded) component is  $\leq 2 \times 10^4 \text{ cm}^{-3}$  at the innermost points, and falls off monotonically with radial distance. We have held U roughly constant for this component within the inner  $1''$  ( $\sim 100$  pcs), allowing it to drop for the outermost points. The ionization parameter for the matter-bounded component was allowed to vary to produce the best fit to the observed emission-line ratios when its contribution was added to

that of the radiation-bounded component, however, its density is also a decreasing function of radial distance. The component-weighted model densities as a function of radial distance are plotted in Figure 4, along with power law fits, showing that density falls off as  $n_H \propto r^{-s}$ , where  $s = -1.6$  to  $-1.7$ . The one exception to the two-component scheme is position  $0''.1 - 0''.3$  NE, for which three components were required, which might be expected since projection effects are likely to be greatest at small projected radial distances.

## 5. Model Results

The model results are shown graphically in Figures 5 and 6. As a measure of the goodness of the fit, we have included dotted lines to mark a factor of two divergence between the model prediction and the observed line strength. Given the simplicity of the models, the fact that the large majority of the emission lines are well fit validates our basic assumption, e.g. that photoionization is the dominant mechanism for ionizing the NLR gas, and that the densities, dust fraction and abundances used for the models are approximately correct. Also, our estimated central source luminosity is sufficient to power the NLR, which implies that 1) there is no evidence for anisotropy of the continuum radiation, and 2) the average luminosity of the central source has been roughly the same for several hundreds of years. Furthermore, by fitting lines from ions with a wide range of ionization potential (e.g., 7.6 eV for Mg II; 97.0 eV for Ne V) the model predictions confirm that the SED of the ionizing continuum is correct, including the assumptions regarding the effects of the UV and X-ray absorbers.

### 5.1. Fit to the Observations

As expected, we have achieved good fits simultaneously for the strengths of C IV  $\lambda 1550$ , [O III]  $\lambda 5007$ , [O II]  $\lambda 3727$ , and He II  $\lambda 4686$ , relative to  $H\beta$ . Even though we weighted the contributions of the individual components bases on these lines, the quality of the fit indicates that we have made a good approximation to the range of physical conditions at each point. Also, the composite models give good predictions for high ionization lines, such as O IV]  $\lambda 1402$  and [Ne V]  $\lambda 3426$ , and lower ionization lines, including those formed primarily in the  $H^+$  zone, such as [Ne III]  $\lambda\lambda 3869, 3968$  and [N II]  $\lambda\lambda 6548, 6584$ , and those formed in the  $H^0$  zone, such as [O I]  $\lambda\lambda 6300, 6364$ , [N I]  $\lambda\lambda 5198, 5200$ , and [S II]  $\lambda\lambda 6716, 6731$ . Not only does the quality of the fit further validate our simple two component scheme but, also, the fact that lines from the neutral envelopes are well-fit supports the assumption that much of the NLR gas is radiation-bounded.

Our central hypothesis was that the NLR was irradiated by an ionizing continuum which was absorbed by intervening gas close to the nucleus. As noted above, the fit to SED sensitive lines, such as He II  $\lambda 4686$ , and lines from a wide range of ionization states indicate that the overall SED is approximatedly correct. The electron temperature is also sensitive to assumptions about the SED. For the models of the bins NE of the nucleus, the predicted ratio of [O III]  $\lambda 4363$ /[O III]  $\lambda 5007$  is, on average, within a factor of  $\approx 1.5$  of that observed, which indicates a reasonably accurate prediction for the electron temperature. The relative strength of [O III]  $\lambda 4363$  is somewhat underpredicted in the models for the bins SW of the nucleus. We take this as an indication that we somewhat overestimated the absorption at energies greater than 100 eV, which is primarily due to the X-ray absorber (see Figure 3). Since the strength of [O I]  $\lambda 6300$  is sensitive to the electron temperature in the  $H^0$  zone, the underprediction of [O I]  $\lambda 6300$  in the SW is additional evidence that we have overestimated of the continuum absorption in the X-ray. Nevertheless, the main point is that the relative



suppression of the He II line strength in gas with a fairly high state of excitation indeed results from ionization by a continuum which has a paucity of photons near the He II Lyman limit, as suggested by Alexander et al. (1999) and Kraemer et al. (1999), and that it appears that the much of the NLR in NGC 4151 sees the same continuum.

In Figure 7 we compare the observed ratio of [S II]  $\lambda 6716/\lambda 6731$  to that predicted by the models. The observed ratio shows a general increase with radial distance, also seen in the model results, indicating a fall-off in electron density (Osterbrock 1989). The models overpredict the value of the  $\lambda 6716/\lambda 6731$  ratio for several bins, particularly those closest to the nucleus, which is evidence that the actual densities are greater than those assumed for the models, although the differences are generally a factor of a few. This may result from our assumption of constant density for each component, since it is certainly plausible that the inner regions of the clouds are somewhat denser than the hotter, ionized outer parts, whether or not the clouds are pressure confined. Regarding pressure confinement, the two components are not in pressure equilibrium with one another, since the densities generally differ by factors of  $\sim 30$  (see Table 3), while the temperatures differ by factors of  $\sim 2$  (see Table 4). The simplest explanation is that the clouds are not fully pressure confined and are expanding as they traverse the NLR, which may be a natural explanation for the drop in density as a function of radial distance.

As noted in Section 3, the dereddened  $L\alpha/H\beta$  ratios for some regions show the effects of resonance scattering and subsequent destruction of the  $L\alpha$  photons by dust mixed in with the emission-line gas. Kraemer & Harrington (1986) discussed the importance of this process in the NLR of the Seyfert 2 galaxy Mrk 3, but with the current data we also gain insight into the geometry of the NLR of NGC 4151. As we have discussed, to calculate the effects of looking at the back-ends of the clouds, we have made the simple assumption that their physical size is no larger than that defined by our models. Based on our predictions

for the  $L\alpha/H\beta$  ratio for bins  $0''.9 - 0''.1.1$  SW,  $1''.1 - 1''.5$  SW, and  $1''.9 - 2''.3$  SW (see Figure 5), there is no evidence that these  $L\alpha$  photons have a longer path length prior to escape. However, back-end escape greatly underpredicts the resonance lines formed in the neutral envelope of the radiation-bounded component, specifically Mg II  $\lambda 2800$  and C II  $\lambda 1335$ . In each case, the models predictions of the relative strengths of these lines are within the errors if we calculated the escape out the front-end of the clouds. Therefore, either the clouds are not as physically thick as we have assumed or there is a sufficient velocity gradient across the cloud that our assumptions about line profile and frequency shift (see Kraemer 1985) are no longer correct. In any case, based on our results for  $L\alpha$ , the photon path length, dust fraction internal to the clouds and viewing aspect that we have assumed are all approximately correct. Also, there are several other clouds (bins  $0''.5 - 0''.7$  SW,  $1''.5 - 1''.9$  SW,  $0''.3 - 0''.5$  NE, and  $0''.9 - 1''.1$  NE) for which there is some suppression of  $L\alpha$  (see Tables 1 and 2), although it is less extreme than in the cases we have addressed. This can be attributed to either an oblique viewing angle through the cloud or a back-end view through a smaller column of radiation-bounded gas, although, based on the strengths of the collisionally excited lines formed in the neutral envelopes, there is no evidence for the latter. As noted, the facts that the suppression of  $L\alpha$  is much greater in the SW and is due to the effects on internal dust support our previous conclusions regarding the narrow-line kinematics (Hutchings et al. 1998), specifically that the narrow-line clouds in the inner  $\sim 200$  pc are in radial outflow from the nucleus.

In Table 3 we list the total column densities for the component models, which tend to be less than  $2 \times 10^{21} \text{ cm}^{-2}$ . The actual column of hydrogen which line photons traverse while escaping the clouds is typically much less, since the emission-line are formed throughout the cloud, rather than strictly at either the surface or deepest point. On the other hand, the average reddening over the inner  $3''$ ,  $E_{B-V} \approx 0.18$ , indicates that we are observing the emission-lines through columns of at least  $2.5 \times 10^{21} \text{ cm}^{-2}$ , given the dust fraction assumed

and the relationship between hydrogen column density and reddening determined for the Milky Way (Shull & Steenberg 1985). Therefore, the emission-lines are more reddened than can be accounted for by the dust in the clouds in which they are formed (which is why we compared our model predictions to the dereddened line ratios in the first place). Instead, we are either viewing the clouds through a nonuniform external screen, since the reddening varies, or there are multiple dusty clouds along our line-of-sight in many cases, such that the further ones are reddened by the dust in those nearer. There is another compelling reason to believe we are seeing superposition of clouds, which will be discussed in section 5.2.

We have assumed solar abundances for these models and, for all but one of the regions modeled, there are no discrepancies between the model predictions and the observations that could be attributable to differences in the abundances. The one exception is the blue-shifted core ( $0''.1 - 0''.3$  SW), whose spectrum shows relatively strong lines of [Fe VII] ( $\lambda 6087$ ,  $\lambda 5721$ ,  $\lambda 3760$ , and  $\lambda 3588$ ). The model underpredicts these lines by a factor of  $\sim 5$ , although the fit for [Ne V]  $\lambda\lambda 3426, 3346$ , which should arise in similar conditions, is good. We achieved a reasonable fit for the [Fe VII] line by running a test model in which the iron abundance was increased by a factor of 2 and no iron was depleted onto grains. Therefore, we suggest that the fraction of iron in gas phase is higher in this region, perhaps due to a liberation of iron from dust grains combined with a higher iron abundance. There is evidence for iron enhancement in the nucleus of NGC 1068 (Netzer & Turner 1997; Kraemer et al. 1998), so it is not surprising that a similar effect is seen in the inner NLR of NGC 4151.

## 5.2. Open Issues

Although the match between the model predictions and the observations are generally good, there are several apparent discrepancies. First of all, the predictions for the N V  $\lambda 1240$  are generally low. This line is somewhat suppressed due to the resonance scattering-dust destruction process discussed previously. If the dust is not uniformly distributed in the more tenuous components, we might expect to see less suppression of N V  $\lambda 1240$  than the other strong resonance lines, for example C IV  $\lambda 1550$ , since the N<sup>+4</sup> zone in these models does not fully overlap the C<sup>+3</sup> zone and is nearer the illuminated surface of the cloud. Another possible explanation is that the N V line is enhanced through scattering of continuum radiation by N<sup>+4</sup> ions (cf. Hamann & Korista 1996), an effect which is not included in our photoionization code. This effect is particularly important if there is significant turbulence in the clouds. Finally, the N V  $\lambda 1240$  line may arise in gas that is not modeled in our simple two-component scheme. For example, it is possible that there is an even more tenuous, more highly ionized component ( $U \sim 1.0$ ) filling the narrow-line region. If the narrow-line clouds are driven outward by a wind originating in the inner nucleus (cf. Krolik & Begelman 1986), it may be that the N V emission arises in the wind itself. The models also underpredict the C II  $\lambda 1335$  strength, which is most likely due to enhancement by resonance scattering of continuum emission, particularly since the models predict columns of C<sup>+</sup> for the radiation-bounded components typically  $\geq 10^{18} \text{ cm}^{-2}$  for the clouds within 100 pc of the nucleus. Heckman et al. (1997) have found evidence for this effect in the spectrum of the Seyfert 2 galaxy I Zw 92 (Mrk 477). The line may also be affected by the way in which the reddening correction is determined, as we discuss below.

As can be seen from the ratios of the model/observed line strengths plotted in Figures 5 and 6, lines in the near UV band (1700 – 3000 Å ) show what may be a systematic trend. There are a large number of regions for which C III]  $\lambda 1909$ , C II]  $\lambda 2326$  and [Ne IV]  $\lambda 2423$

are unpredicted, particularly on the SW side of the nucleus. Since these lines arise the same physical conditions as several well-fit optical lines (e.g. [O III]  $\lambda 5007$ , [N II]  $\lambda\lambda 6548, 6584$ , etc.) it is unlikely that their underprediction indicates the presence of another component of gas. The fact that the problem is worse in the SW points to the reddening correction as the cause, since we are observing those clouds through a larger column of dust, much of it internal to the emission-line clouds. However, the problem appears to be specific to the near UV band, since there are no apparent systematic discrepancies in the far UV spectra (1200 – 1700 Å ). If the strength of the 2200 Å feature in the interstellar medium of NGC 4151 is less than that in the Milky Way, we may have overestimated the intrinsic strength of the C II]  $\lambda 2326$  and [Ne IV]  $\lambda 2423$  lines. Another explanation is required for the discrepant C III]  $\lambda 1909$  predictions. It is interesting to note that those regions with the worst fit for the C III] line (bins  $0''.5 - 0''.7$  NE,  $0''.3 - 0''.5$  SW,  $0''.7 - 0''.9$  SW, and  $0''.9 - 1''.1$  SW) have reddening corrected  $H\alpha/H\beta$  ratios somewhat below Case B ( $\sim 2.9$ ; Osterbrock 1974), which implies that these lines have been overcorrected for extinction. The problem may be the manner in which the reddening is determined, specifically from the ratio of He II  $\lambda 1640$ /He II  $\lambda 4686$ . We have assumed that the He II lines are viewed through the same column of dust as the other emission lines. This may not be a robust assumption, since most of the He II emission comes from the matter-bounded components. Unfortunately, the physical sizes and geometry of the emitting regions are not well-constrained by our simple models, so it is not possible to quantify this effect. In any case, it is likely that the combined effects of the uncertainty in the extinction curve in NGC 4151 and different viewing angles through inhomogeneous emission-line regions account for these discrepancies.

In Table 4, we list the model predictions for the  $H\beta$  flux emitted at the illuminated face of the cloud. We estimate the size of the emitting area, also given in Table 4, by dividing the observed  $H\beta$  luminosity by the emitted flux. For the matter-bounded clouds, this area tends to be larger than the projected area of the bin, which suggests 1) clouds with larger

depths in the line of sight, or 2) multiple clouds along the line of sight. We also estimate the depths of the emitting regions by dividing these areas by the slit width (10 pc). Within the inner 100 pc, the depths are not greater than the apparent radial distance, and are therefore reasonable in our estimation. At larger radial distances, the emitting area for the matter-bounded component becomes quite large, and would imply that we are seeing the sum of emission from up to several hundreds of parsecs into the galaxy. Note, however, that we arbitrarily truncated the size of the matter-bounded components. Increasing their column densities would result in a decrease in the size of the required emitting area. Therefore, the model predictions may be an overestimate of the depth into the galaxy.

One minor problem with the models is that they generally overpredict the strength of the [S III]  $\lambda 9069$  and  $\lambda 9532$  lines. Osterbrock, Tran, & Veilleux (1992) discussed this problem in the context of the spectral properties of a sample of Seyfert galaxies and suggested that the observed weakness of these lines may indicate a relative underabundance of sulfur. However, accurate dielectronic recombination rates have not yet been calculated for sulfur (Ali et al. 1991) and, as a result, the model predictions may not be reliable (in fact, it is not clear what rates were used by Stasinska (1984), whose results were used by Osterbrock et al.). For this dataset, the problem with the [S III] lines may be instrumental. Using the G750L grating with the STIS CCD at these wavelengths produces an instrumentally generated interference, or “fringing”, pattern (Plait & Bohlin 1998). In our data, the fringing, coupled with the method for subtracting the scattered nuclear spectrum, appears to have caused a certain amount of destructive interference: we estimate that the observed strengths of the [S III] lines have been underestimated by as much as a factor of two at some locations. Given this, we do not see that overprediction of the lines is a problem. The fringing effects can be corrected using a contemporaneous CCD flat-field exposure; we will have this in our subsequent STIS observations of NGC 4151, and will re-evaluate the [S III] problem at that time.

## 6. Implications for the Absorbers

We have shown that the NLR of NGC 4151, at least along one position angle, is ionized by an absorbed continuum, and, thus, there are important implications regarding the distribution of gas in the inner nuclear regions of the galaxy. We should note that we have not placed stringent constraints on the location of the absorber. Specifically, we have not yet discussed the possibility that the absorption could be due to the narrow-line clouds themselves. However, there are good reasons to reject such a model. We obtained a good fit to the emission-line ratios at each radial point assuming that much of the gas is optically thick to the ionizing radiation, at both the He II and hydrogen Lyman limits, unlike the gas that is producing the UV absorption, which is optically thick only at the He II Lyman limit. The one location where there may be evidence for a component with physical conditions similar to the UV absorber is the red-shifted core ( $0''.1 - 0''.3$  NE), specifically the high density, matter-bounded component (see Table 3). However, at the radial distance of this component ( $\geq 4$  pc from the nucleus) the covering factor is  $\ll 0.01$ , assuming an ionization cone with an opening angle of  $75^\circ$  (Evans et al. 1993), so there could be no effect on clouds further out. It is possible that the X-ray absorber extends further into the NLR, and we have argued that there may be a component of high ionization, tenuous gas that contributes some of the N V emission. However, we estimate from U and the size of the emitting regions that the column densities of such a component could not be much greater than a few  $\times 10^{21}$   $\text{cm}^{-2}$ , and, therefore, insufficient to produce the depth of the absorption features in the X-ray required for our models. Furthermore, we do not see any trends with radial distance, such as weaker neutral lines or [O III]  $\lambda 4363$  emission, that would indicate a drop in electron temperature, and thus an increasing column of X-ray absorber. Thus, it is most likely that both the UV and X-ray absorbers lie within a few parsecs of the nucleus, as is apparently the case for the absorbers along our line-of-sight.

Based on the fraction of Seyferts found to possess UV and X-ray absorption, the absorber must have a covering factor between 0.5 – 1.0 (Crenshaw et al. 1999). Our analysis suggests that, along the position angle of these data, the absorber covers the lines of sight to the NLR, which is in agreement with the average NLR conditions in NGC 4151 discussed by Alexander et al. (1999). Unfortunately, we cannot determine the distribution of NLR gas into the plane of the galaxy from the current dataset, as we noted in the Section 5.1, although there are likely to be large projection effects. We have medium resolution ( $\lambda/\Delta\lambda \approx 10,000$ ) slitted observations planned with *HST*/STIS which may provide better constraints on the distribution of the narrow-line gas and help resolve this question.

## 7. Conclusions

We have examined the physical conditions, along PA 221°, in the narrow-line gas in the inner  $\sim 250$  pc of the Seyfert 1 galaxy NGC 4151, using low resolution, long slit data obtained with *HST*/STIS. We have measured the emission-line fluxes at contiguous radial points along the slit, performed reddening corrections based on the He II  $\lambda 1640/\lambda 4686$  ratio, and compared the results with the predictions of detailed photoionization models. The main results are as follows:

1. The conditions in the NLR gas are the result of photoionization by continuum radiation emitted by the central active nucleus. If additional excitation mechanisms are present, such as shocks or interaction between the radio jet and the interstellar gas, the effects must be quite subtle, since the heating and ionization of the gas can be successfully modeled by photoionization effects. Note, however, that this position angle does not lie directly along the radio jet (see Kaiser et al. 1999, and references therein).
2. It is clear that we are also seeing the effects of dust imbedded in the clouds.



Specifically, the  $L\alpha/H\beta$  ratio on the SW side of the nucleus is much lower than predicted by the combination of recombination and collisional excitation, and is almost certainly due to line transfer effects within dusty gas. The simplest interpretation is that the clouds on the SW are viewed out the back-end, rather than from the illuminated face. We used the photoionization models to explore this effect and have demonstrated that the column densities and dust fraction that we assumed can produce the observed suppression of  $L\alpha$ . This is further proof that the clouds in the inner NLR are outflowing radially from nucleus, with the SW side approaching us and the NE side receding from us, as discussed in our previous papers (Hutchings et al. 1998; Kaiser et al. 1999).

Although our model predictions indicate that the fraction of dust within the emission-line gas is roughly constant across the NLR, the amount of reddening varies. Although this could be due to variations in the column density of an external dust screen, it can also be the result of stacking of NLR clouds along our line-of-sight. We prefer the latter explanation, since there is evidence, based on the predicted  $H\beta$  fluxes, that we are seeing the superposition of clouds.

3. We have confirmed the earlier results of Kraemer et al. (1999) and Alexander et al. (1999), which indicated that the ionizing continuum which irradiates the NLR in NGC 4151 has been absorbed by an intervening layer of gas close to the nucleus. With these models we have put much more realistic constraints on the SED of the transmitted continuum. The fact that the NLR sees an absorbed continuum implies that the covering factor of the absorbing material is large, as Crenshaw et al. (1999) have suggested.

S.B.K. and D.M.C acknowledge support from NASA grant NAG 5-4103.

## REFERENCES

- Alexander, T., Sturm, E., Lutz, D., Sternberg, A., Netzer, H., & Genzel, R. 1999, *ApJ*, 512, 204
- Ali, B., Blum, R.D., Bumgardner, T.E., Cranmer, S.R., Ferland, G.J., Haefner, R.I., & Tiede, G.P. 1991, *PASP*, 103, 1182
- Arnaud, K.A., et al. 1985, *MNRAS*, 217, 105
- Barr, P., White, N.E., Sanford, P.W., & Ives, J.C. 1977, *MNRAS*, 181, 43P
- Binette, L., Robinson, A., & Courviosier, T.J-L. 1988, *A&A*, 194, 65
- Bromage, G.E., et al. 1985, *MNRAS*, 251, 1
- Capriotti, E., Foltz, C., & Byard, P. 1979, *ApJ*, 230, 681
- Cohen, M., Harrington, J.P., & Hess, R. 1984, *ApJ*, 283, 687
- Crenshaw, D.M., Kraemer, S.B., Boggess, A., Maran, S.P, Mushotzky, R.F., & Wu, C.-C. 1999, *ApJ*, 516, 750
- de Robertis, M.M., & Osterbrock, D.E. 1984, *ApJ*, 286, 171
- Edelson, R.A., et al. 1996, *ApJ*, 470, 364
- Espey, B.R., Kriss, G.A., Krolik, J.H., Zheng, W., Tsvetanov, Z., Davidsen, A.F. 1998, *ApJ*, 500, L13
- Evans, I.N., Tsvetanov, Z., Kriss, G.A., Ford, H.C., Caganoff, S., & Koratkar, A.P. 1993, *ApJ*, 417, 82
- Grevesse, N., & Anders, E. 1989, in *AIP Conf. Proc.* 183, *Cosmic Abundances of Matter*, ed. C.J. Waddington (New York: AIP), 1
- Hamann, F., & Korista, K.T. 1996, *ApJ*, 464, 158

- Heckman, T.M., Gonzalez-Delgado, R., Leitherer, C., Meurer, G.R., Krolik, J., Wilson, A.S., Koratkar, A., & Kinney, A. 1997, *ApJ*, 482, 114
- Holt, S.S., Mushotzky, R.F., Becker, R.H., Boldt, E.A., Serlemitsos, P.J., Szymkowiak, A.E., & White, N.E. 1980, *ApJ*, 241, L13
- Hutchings, J.B., et al. 1998, *ApJ*, 492, L115
- Kaiser, M.E., et al. 1999, *ApJ*, in press
- Korista, K.T., & Ferland, G.J. 1989, *ApJ*, 343, 678
- Kraemer, S.B. 1985, Ph.D. thesis, Univ. Maryland
- Kraemer, S.B., & Harrington, J.P. 1986, *ApJ*, 307, 478
- Kraemer, S.B., Ruiz, J.R., & Crenshaw, D.M. 1998, *ApJ*, 508, 232
- Kraemer, S.B., Turner, T.J., Crenshaw, D.M., & George, I.M. 1999, *ApJ*, 519, 69
- Kraemer, S.B., Wu, C.-C., Crenshaw, D.M., & Harrington, J.P. 1994, *ApJ*, 435, 171
- Kriss, G.A., et al. 1992, *ApJ*, 392, 485
- Kriss, G.A. 1998, in *The Scientific Impact of the Goddard High Resolution Spectrograph*, ed. J.C. Brandt, T.B. Ake, & C.C. Petersen (San Francisco: Astronomical Society of the Pacific), ASP Conference Series, 143, 271
- Kriss, G.A., Davidsen, A.F., Zheng, W., Kruk, J.W., & Espey, B.R. 1995, *ApJ*, 454, L7
- Krolik, J.H., & Begelman, M.C. 1986, *ApJ*, 308, L55
- Mushotzky, R.F., Holt, S.S., & Selemitsos, P.J. 1978, *ApJ*, 225, L115
- Nelson, C.H., et al. 1999, in preparation
- Netzer, H. 1997, *Ap&SS*, 248, 127
- Netzer, H., & Turner, T.J. 1997, *ApJ*, 488, 694
- Osterbrock, D.E. 1974, *Astrophysics of Gaseous Nebulae* (San Francisco: W. H. Freeman)

- Osterbrock, D.E. 1989, *Astrophysics of Gaseous Nebulae and Active Galactic Nuclei* (Mill Valley, Univ. Science Books)
- Osterbrock, D.E., Tran, H.D., & Veilleux, S. 1992, *ApJ*, 389, 196
- Penston, M.V., & Perez, E. 1984, *MNRAS*, 211, 33P
- Plait, P., & Bohlin, R. 1998, in *The 1997 HST Calibration Workshop With a New Generation of Instruments*, ed. S. Casertano, R. Jedrzejewski, C.D. Keyes, & M. Stevens (Baltimore: Space Telescope Science Institute), 150
- Savage, B.D., & Mathis, J.S. 1979, *ARA&A*, 17, 73
- Schmitt, H.R., & Kinney, A.L. 1996, *ApJ*, 463, 498
- Schulz, H., & Komossa, S. 1993, *A&A*, 278, 29
- Shull, J.M., & Van Steenberg, M.E. 1985, *ApJ*, 294, 599
- Seab, C.G., & Shull, J.M. 1983, *ApJ*, 275, 652
- Seaton, M.J. 1978, *MNRAS*, 185, 5P
- Stasinska, G. 1984, *A&A*, 135, 341
- Turner, T.J. et al. 1999, *ApJ*, 510, 178
- Warwick, R.S., Done, C., & Smith, D.A. 1995, *MNRAS*, 275, 1003
- Weaver, K.A., Yaqoob, T., Holt, S.S., Mushotzky, R.F., Matsuoka, M., & Yamauchi, M. 1994, *ApJ*, 436, L27
- Weymann, R.J., Morris, S.L., Gray, M. E., & Hutchings, J.C. 1997, *ApJ*, 483, 717
- Wilson, A.S., & Raymond, J.C. 1999, *ApJ*, 513, L115
- Wilson, A.S., & Ulvestad, J.S. 1982, *ApJ*, 263, 576

Yaqoob, T., Warwick, R.S., & Pounds, K.A. 1989, MNRAS, 236, 153

Table 3. Model Parameters

Bin	U	hydrogen density ( $\text{cm}^{-3}$ )	column density ( $\text{cm}^{-2}$ )	fraction of $\text{H}\beta$ emission	notes <sup>a</sup>
0".1 – 0".3 SW	$10^{-2.63}$	$1.8 \times 10^4$	$1.3 \times 10^{21}$	0.70	RB
	$10^{-1.12}$	$6.6 \times 10^2$	$4.1 \times 10^{20}$	0.30	MB
0".3 – 0".5 SW	$10^{-2.63}$	$1.2 \times 10^4$	$1.3 \times 10^{21}$	0.70	RB
	$10^{-1.12}$	$3.7 \times 10^2$	$5.3 \times 10^{20}$	0.30	MB
0".5 – 0".7 SW	$10^{-2.57}$	$5.0 \times 10^3$	$1.3 \times 10^{21}$	0.80	RB
	$10^{-1.04}$	$1.5 \times 10^2$	$5.6 \times 10^{20}$	0.20	MB
0".7 – 0".9 SW	$10^{-2.64}$	$3.0 \times 10^3$	$1.1 \times 10^{21}$	0.80	RB
	$10^{-1.16}$	$1.0 \times 10^2$	$3.7 \times 10^{20}$	0.20	MB
0".9 – 1".1 SW	$10^{-2.66}$	$2.0 \times 10^3$	$1.0 \times 10^{21}$	0.80	RB
	$10^{-1.3}$	$6.0 \times 10^1$	$3.0 \times 10^{20}$	0.20	MB
1".1 – 1".5 SW	$10^{-2.66}$	$1.2 \times 10^3$	$9.3 \times 10^{20}$	0.90	RB
	$10^{-1.13}$	$3.5 \times 10^1$	$2.8 \times 10^{20}$	0.10	MB
1".5 – 1".9 SW	$10^{-2.82}$	$1.0 \times 10^3$	$7.2 \times 10^{20}$	0.80	RB
	$10^{-1.13}$	$2.0 \times 10^1$	$9.6 \times 10^{19}$	0.20	MB
1".9 – 2".3 SW	$10^{-2.87}$	$7.5 \times 10^2$	$6.3 \times 10^{20}$	0.85	RB
	$10^{-1.15}$	$1.5 \times 10^1$	$1.3 \times 10^{20}$	0.15	MB
0".1 – 0".3 NE	$10^{-2.67}$	$1.2 \times 10^4$	$1.6 \times 10^{21}$	0.50	RB
	$10^{-3.0}$	$1.0 \times 10^7$	$5.6 \times 10^{19}$	0.25	MB
	$10^{-1.08}$	$1.0 \times 10^5$	$5.6 \times 10^{20}$	0.25	MB
0".3 – 0".5 NE	$10^{-2.67}$	$1.2 \times 10^4$	$1.6 \times 10^{21}$	0.90	RB
	$10^{-1.36}$	$6.0 \times 10^2$	$5.3 \times 10^{20}$	0.10	MB
0".5 – 0".7 NE	$10^{-2.61}$	$5.0 \times 10^3$	$1.9 \times 10^{21}$	0.85	RB
	$10^{-1.08}$	$1.5 \times 10^2$	$5.6 \times 10^{20}$	0.15	MB
0".7 – 0".9 NE	$10^{-2.69}$	$3.0 \times 10^3$	$1.3 \times 10^{21}$	0.80	RB
	$10^{-1.2}$	$1.0 \times 10^2$	$4.4 \times 10^{20}$	0.20	MB
0".9 – 1".1 NE	$10^{-2.69}$	$2.0 \times 10^3$	$1.2 \times 10^{21}$	0.90	RB
	$10^{-1.17}$	$6.0 \times 10^1$	$3.3 \times 10^{20}$	0.10	MB
1".5 – 1".9 NE	$10^{-3.0}$	$1.3 \times 10^3$	$7.9 \times 10^{20}$	0.80	RB
	$10^{-1.16}$	$2.0 \times 10^1$	$1.2 \times 10^{19}$	0.20	MB
1".9 – 2".3 NE	$10^{-2.90}$	$7.5 \times 10^2$	$7.7 \times 10^{20}$	0.67	RB
	$10^{-1.3}$	$2.0 \times 10^1$	$2.1 \times 10^{20}$	0.33	MB
2".3 – 2".7 NE	$10^{-2.90}$	$5.3 \times 10^2$	$7.5 \times 10^{20}$	0.75	RB
	$10^{-1.36}$	$1.5 \times 10^1$	$2.2 \times 10^{20}$	0.25	MB

<sup>a</sup>“RB” = radiation-bounded; “MB” = matter-bounded.

Table 4. Selected Model Output Parameters

Bin	U	$T_{initial}^a$	$T_{final}^b$	H $\beta$ flux <sup>c</sup>	area <sup>d</sup>	distance (pc)	distance into plane (pc) <sup>e</sup>
0".1 – 0".3 SW	$10^{-2.63}$	11,750	–	$5.09 \times 10^{-1}$	$8.2^2$	23	7
	$10^{-1.12}$	21,450	18,100	$1.88 \times 10^{-2}$	$28.0^2$	23	78
0".3 – 0".5 SW	$10^{-2.63}$	11,650	–	$3.39 \times 10^{-1}$	$6.7^2$	47	5
	$10^{-1.12}$	21,400	16,900	$1.62 \times 10^{-2}$	$20.0^2$	47	40
0".5 – 0".7 SW	$10^{-2.57}$	11,700	–	$1.61 \times 10^{-1}$	$9.5^2$	67	9
	$10^{-1.04}$	22,200	17,900	$6.6 \times 10^{-3}$	$23.6^2$	67	56
0".7 – 0".9 SW	$10^{-2.64}$	11,200	–	$8.39 \times 10^{-2}$	$10.6^2$	94	11
	$10^{-1.16}$	20,800	17,600	$3.08 \times 10^{-3}$	$27.6^2$	94	76
0".9 – 1".1 SW	$10^{-2.66}$	11,000	–	$5.43 \times 10^{-2}$	$18.3^2$	118	33
	$10^{-1.3}$	21,200	18,600	$1.44 \times 10^{-3}$	$56.1^2$	118	314
1".1 – 1".5 SW	$10^{-2.66}$	10,800	–	$3.22 \times 10^{-2}$	$16.3^2$	153	27
	$10^{-1.13}$	21,200	18,600	$7.96 \times 10^{-4}$	$34.6^2$	153	120
1".5 – 1".9 SW	$10^{-2.82}$	10,000	–	$1.90 \times 10^{-2}$	$22.5^2$	202	23
	$10^{-1.13}$	21,200	19,900	$1.53 \times 10^{-4}$	$125.4^2$	202	769
1".9 – 2".3 SW	$10^{-2.87}$	9,800	–	$1.30 \times 10^{-2}$	$18.8^2$	245	35
	$10^{-1.15}$	20,700	19,100	$1.58 \times 10^{-4}$	$71.5^2$	245	511

Table 4—Continued

Bin	U	$T_{initial}^a$	$T_{final}^b$	H $\beta$ flux <sup>c</sup>	area <sup>d</sup>	distance (pc)	distance into plane (pc) <sup>e</sup>
0".1 – 0".3 NE	$10^{-2.67}$	11,900	–	$3.18 \times 10^{-1}$	$7.0^2$	38	5
	$10^{-3.0}$	13,900	12,800	$5.90 \times 10^2$	$0.1^2$	4	.001
	$10^{-1.08}$	22,300	20,500	$4.26 \times 10^1$	$0.4^2$	4	.02
0".3 – 0".5 NE	$10^{-2.67}$	11,900	–	$3.18 \times 10^{-1}$	$8.5^2$	38	7
	$10^{-1.36}$	22,800	17,600	$1.55 \times 10^{-2}$	$12.8^2$	38	16
0".5 – 0".7 NE	$10^{-2.61}$	12,000	–	$1.51 \times 10^{-1}$	$7.1^2$	55	5
	$10^{-1.08}$	23,600	18,700	$6.29 \times 10^{-3}$	$14.6^2$	55	21
0".7 – 0".9 NE	$10^{-2.69}$	11,500	–	$5.08 \times 10^{-2}$	$15.9^2$	77	25
	$10^{-1.2}$	22,100	17,600	$3.56 \times 10^{-3}$	$30.0^2$	77	90
0".9 – 1".1 NE	$10^{-2.69}$	11,350	–	$5.08 \times 10^{-2}$	$17.2^2$	96	30
	$10^{-1.17}$	22,500	19,100	$1.6 \times 10^{-3}$	$32.2^2$	96	104
1".5 – 1".9 NE	$10^{-3.0}$	10,300	–	$1.78 \times 10^{-2}$	$10.9^2$	165	12
	$10^{-1.16}$	22,600	20,700	$2.0 \times 10^{-4}$	$51.7^2$	165	267
1".9 – 2".3 NE	$10^{-2.90}$	10,300	–	$1.21 \times 10^{-2}$	$14.5^2$	200	21
	$10^{-1.3}$	22,000	20,000	$3.50 \times 10^{-4}$	$60.0^2$	200	360
2".3 – 2".7 NE	$10^{-2.90}$	10,200	–	$8.39 \times 10^{-3}$	$17.6^2$	240	31
	$10^{-1.36}$	20,100	17,300	$2.83 \times 10^{-4}$	$55.3^2$	240	306

<sup>a</sup>electron temperature at the illuminated face of cloud.

<sup>b</sup>electron temperature at the point the model was truncated (matter-bounded models only).

<sup>c</sup>H $\beta$  flux at illuminated face (ergs sec<sup>-1</sup> cm<sup>-2</sup>).

<sup>d</sup>surface area (in pc<sup>2</sup>) required to match observed H $\beta$  luminosity.

<sup>e</sup>emitting area divided by projected slit width (10 pc).



Fig. 1.— Plots of reddening and various dereddened line ratios as a function of projected position from the nucleus. Negative values correspond to the southwest (blueshifted) region.

Fig. 2.— The ionizing continuum assumed for the SW models. The solid line is the intrinsic continuum (see section 4.1). The dotted line shows the effects of transmission through the X-ray absorber ( $U = 1.0$ ,  $N_H = 3.2 \times 10^{22} \text{ cm}^{-2}$ ). The dashed the line shows the combined effects of the X-ray and UV ( $U = 0.001$ ,  $N_H = 2.8 \times 10^{19} \text{ cm}^{-2}$ ) absorbers.

Fig. 3.— The ionizing continuum assumed for the NE models. The solid line is the intrinsic continuum (see section 4.1). The dotted line shows the effects of transmission through the X-ray absorber ( $U = 1.0$ ,  $N_H = 3.2 \times 10^{22} \text{ cm}^{-2}$ ). The dashed the line shows the combined effects of the X-ray and UV ( $U = 0.001$ ,  $N_H = 5.6 \times 10^{19} \text{ cm}^{-2}$ ) absorbers.

Fig. 4.— Weighted density for the two-component models as a function of projected position from the nucleus. The dotted lines are power law fits such that  $n_H \propto r^{-s}$ . Negative values correspond to the southwest (blueshifted) region.

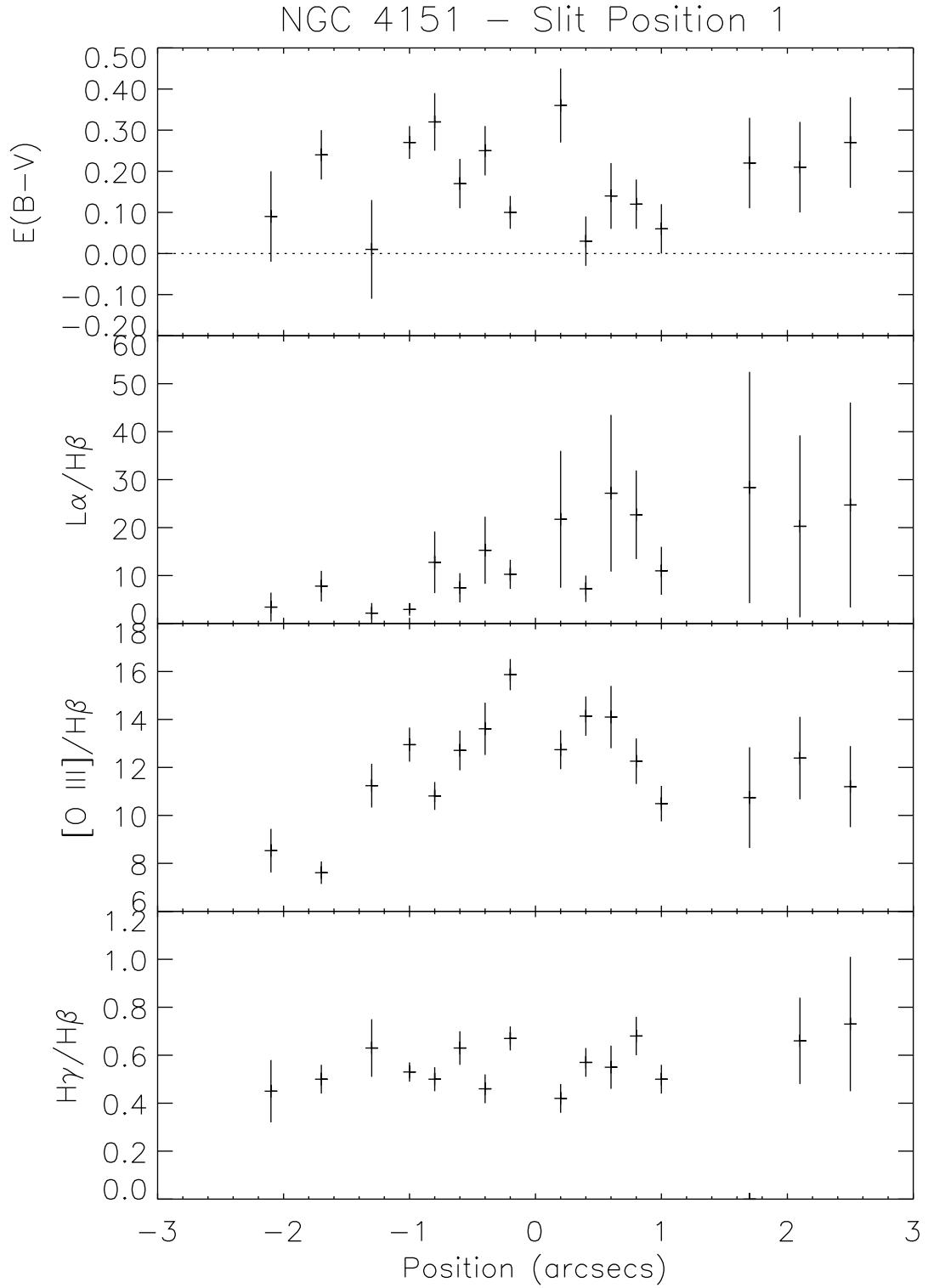
Fig. 5.— The ratios of the model predictions to the observed and dereddened line strengths for the regions southwest of the nucleus. The dashed line indicates a 1:1 correspondence between the predicted and observed values; the dotted lines indicate a factor of two difference. The values for [N I]  $\lambda 5200$  and [S II]  $\lambda 6723$  refer to the combined fluxes of those doublets. The value for C III]  $\lambda 1909$  includes Si III]  $\lambda 1892$ , and C II]  $\lambda 2326$  includes [O III]  $\lambda \lambda 2321, 2332$ .

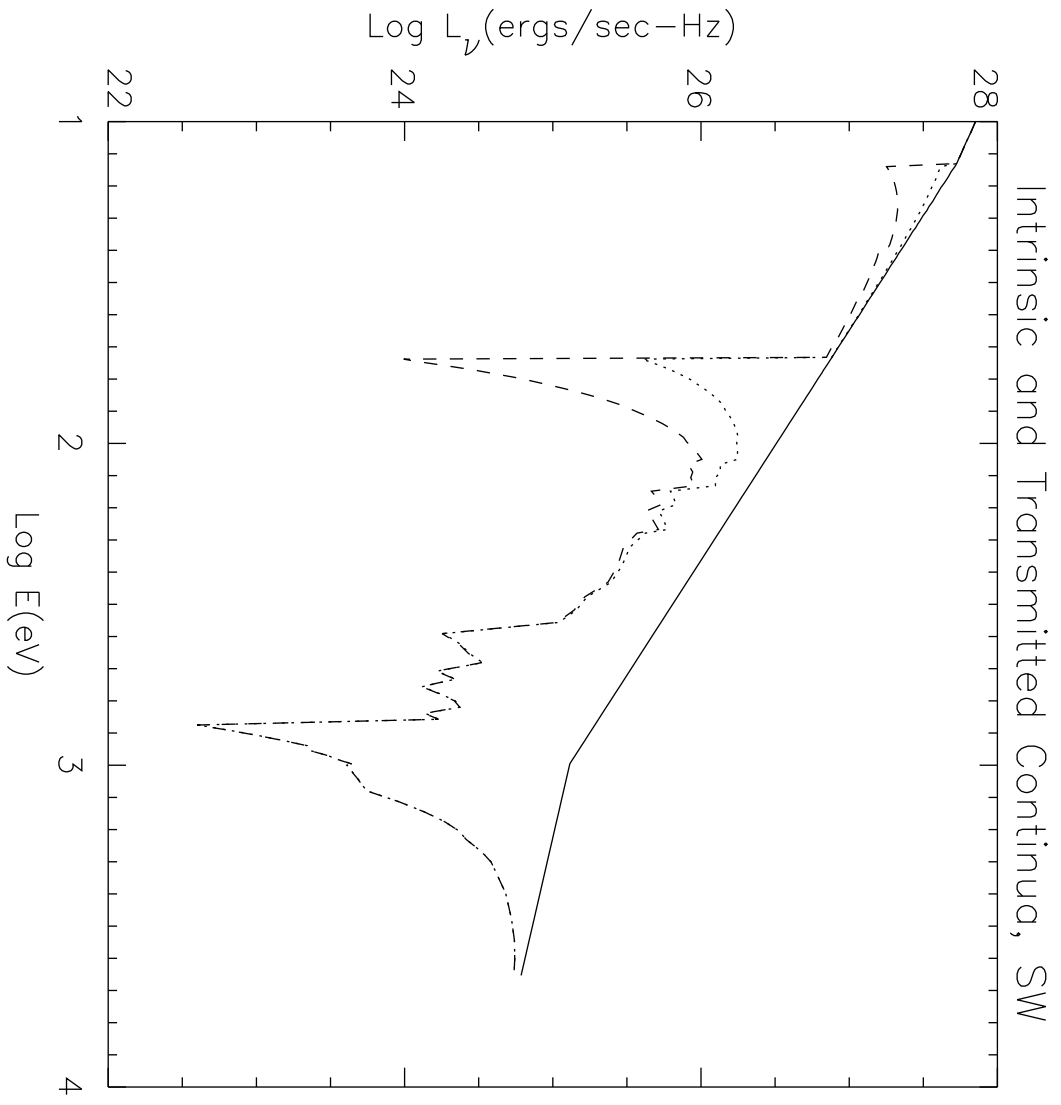
Fig. 6.— The ratios of the model predictions to the observed and dereddened line strengths for the regions northeast of the nucleus (same format as Figure 5).

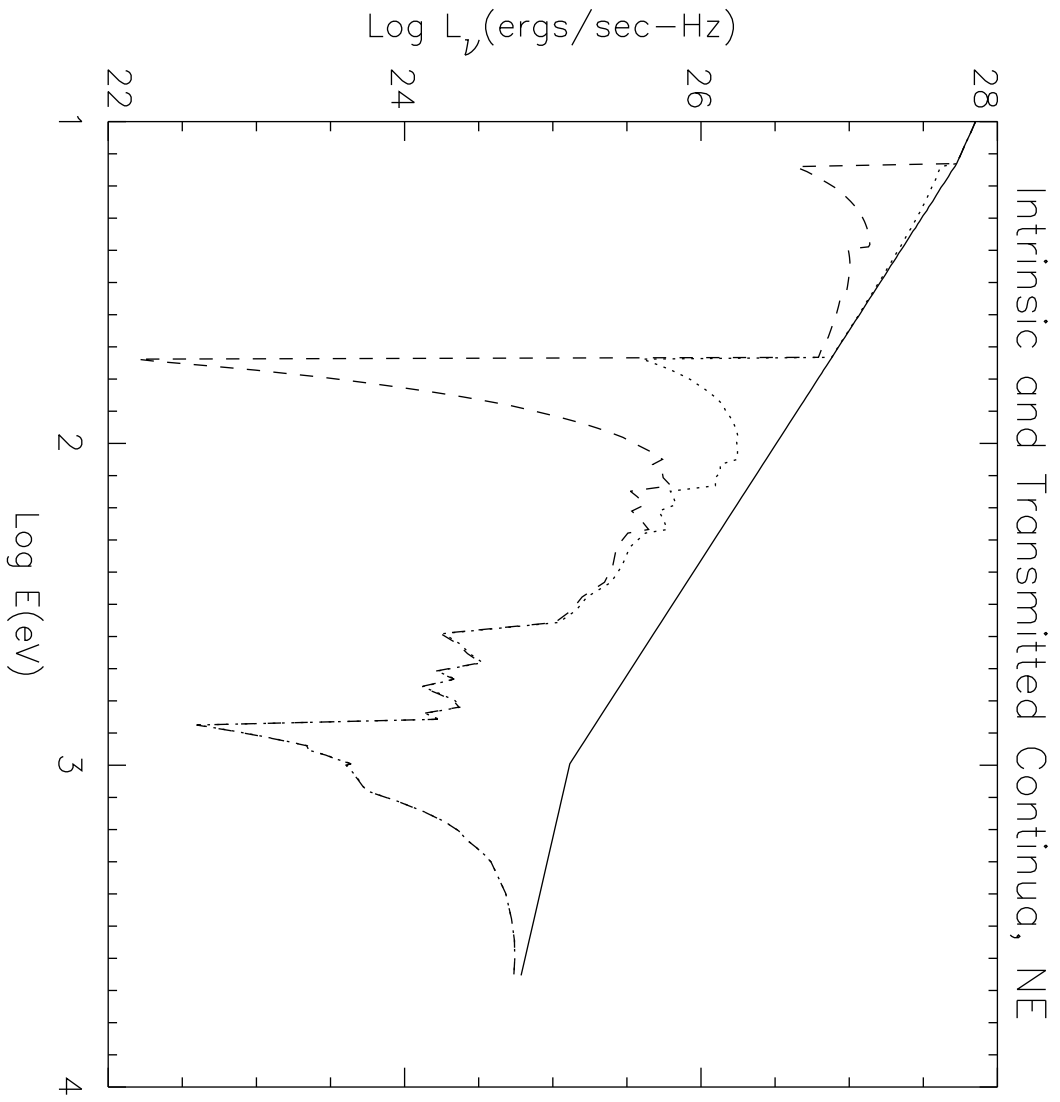
Fig. 7.— Comparison of model predictions (x's) and observed and dereddened values (+'s) of the ratio of [S II]  $\lambda 6716/\lambda 6731$  as a function of projected position from the nucleus. Negative

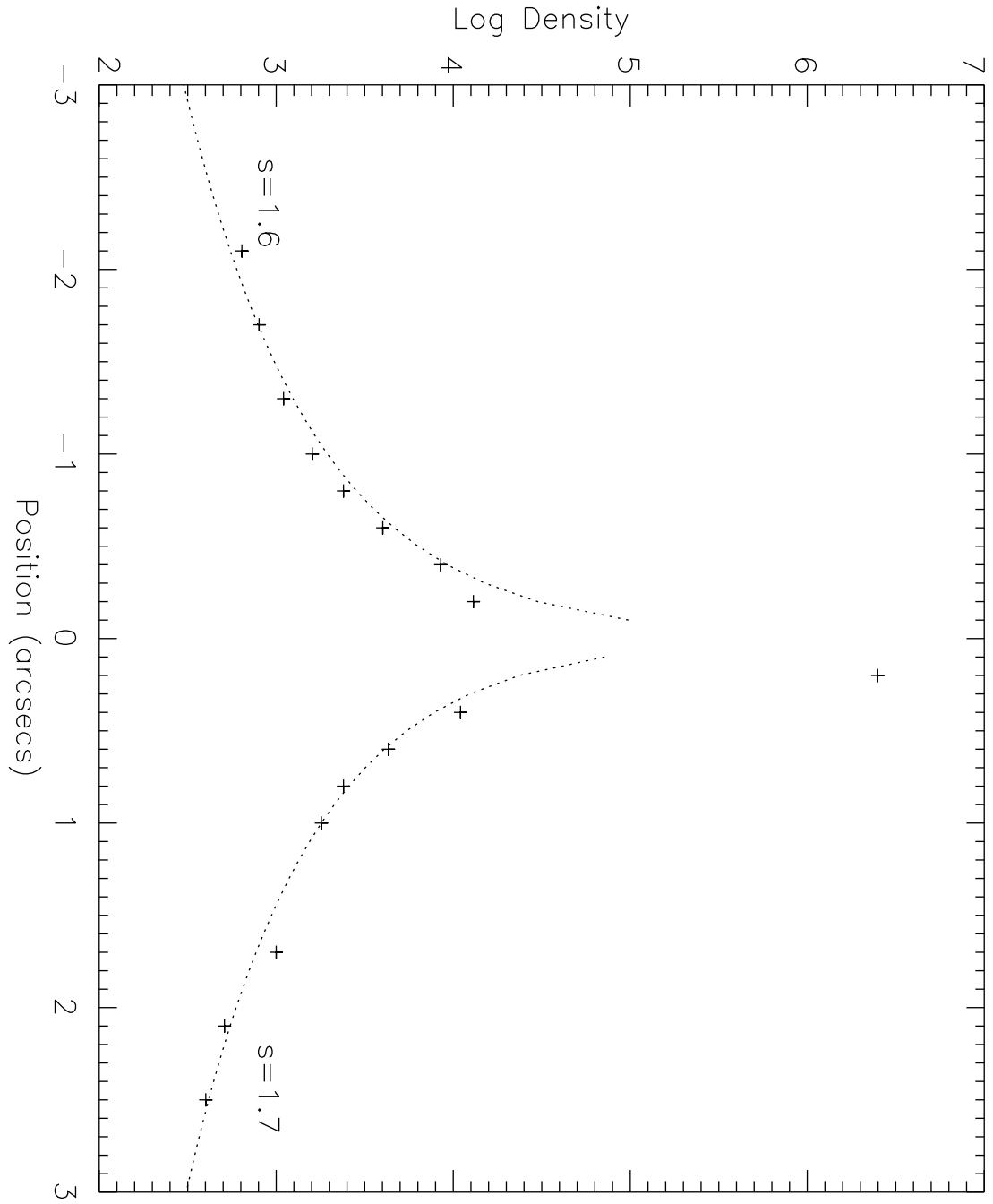
values correspond to the southwest (blueshifted) region. Corresponding electron densities range from  $4 \times 10^3 \text{ cm}^{-3}$  to  $1.8 \times 10^2 \text{ cm}^{-3}$  ( $\lambda 6716/\lambda 6731 = 0.60$  to  $1.25$ ) (Osterbrock 1989).



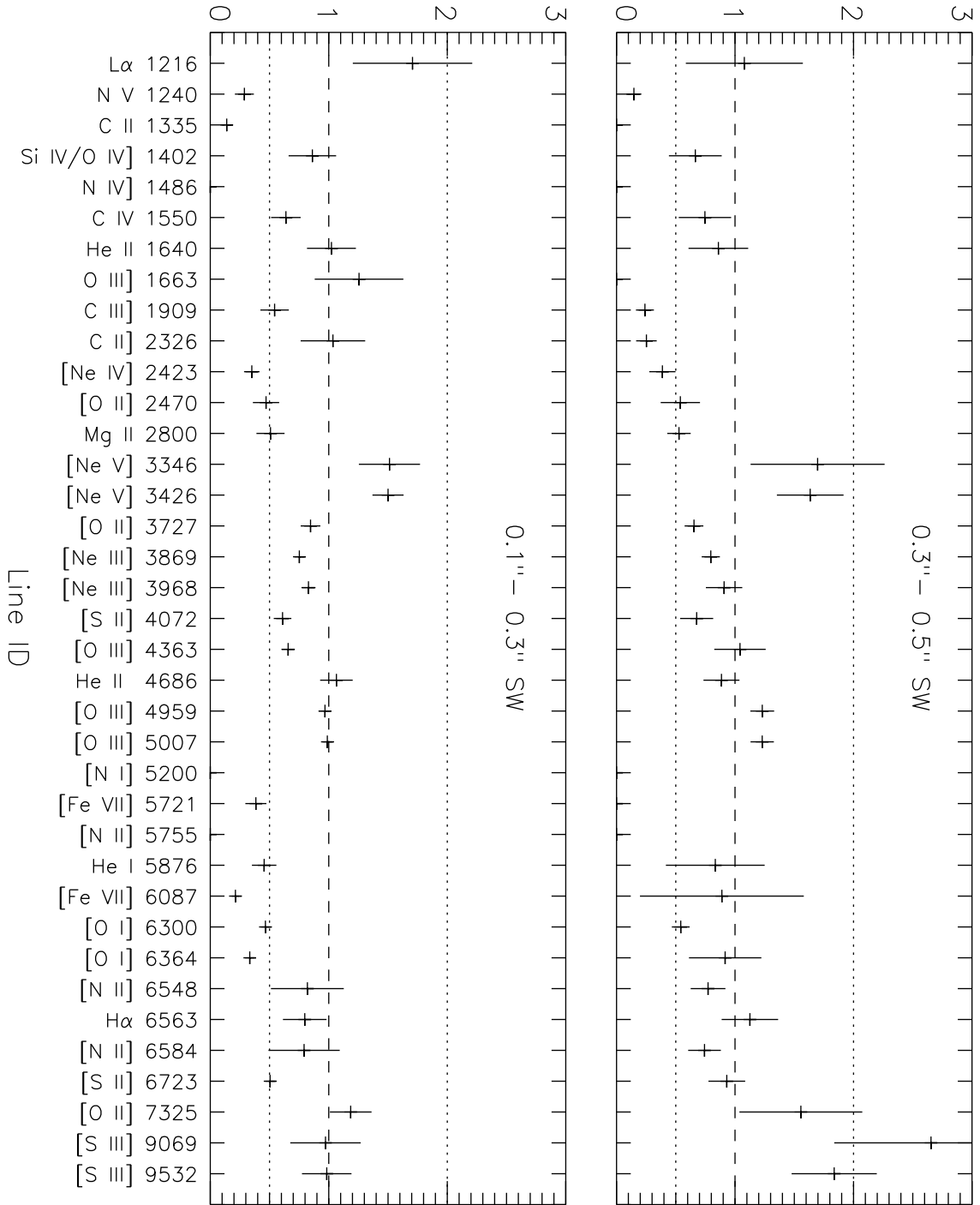






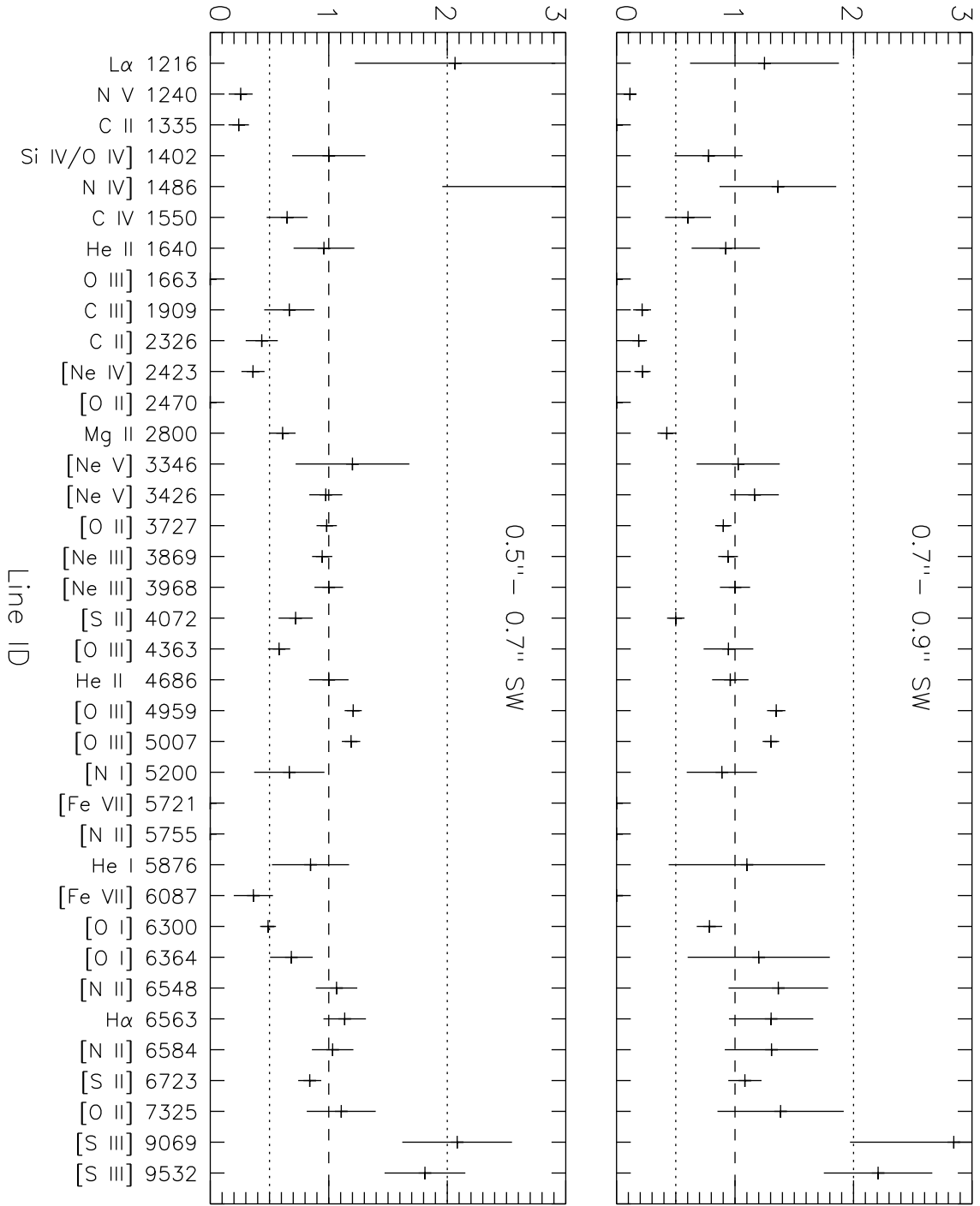


Model Ratio/Dereddened Ratio

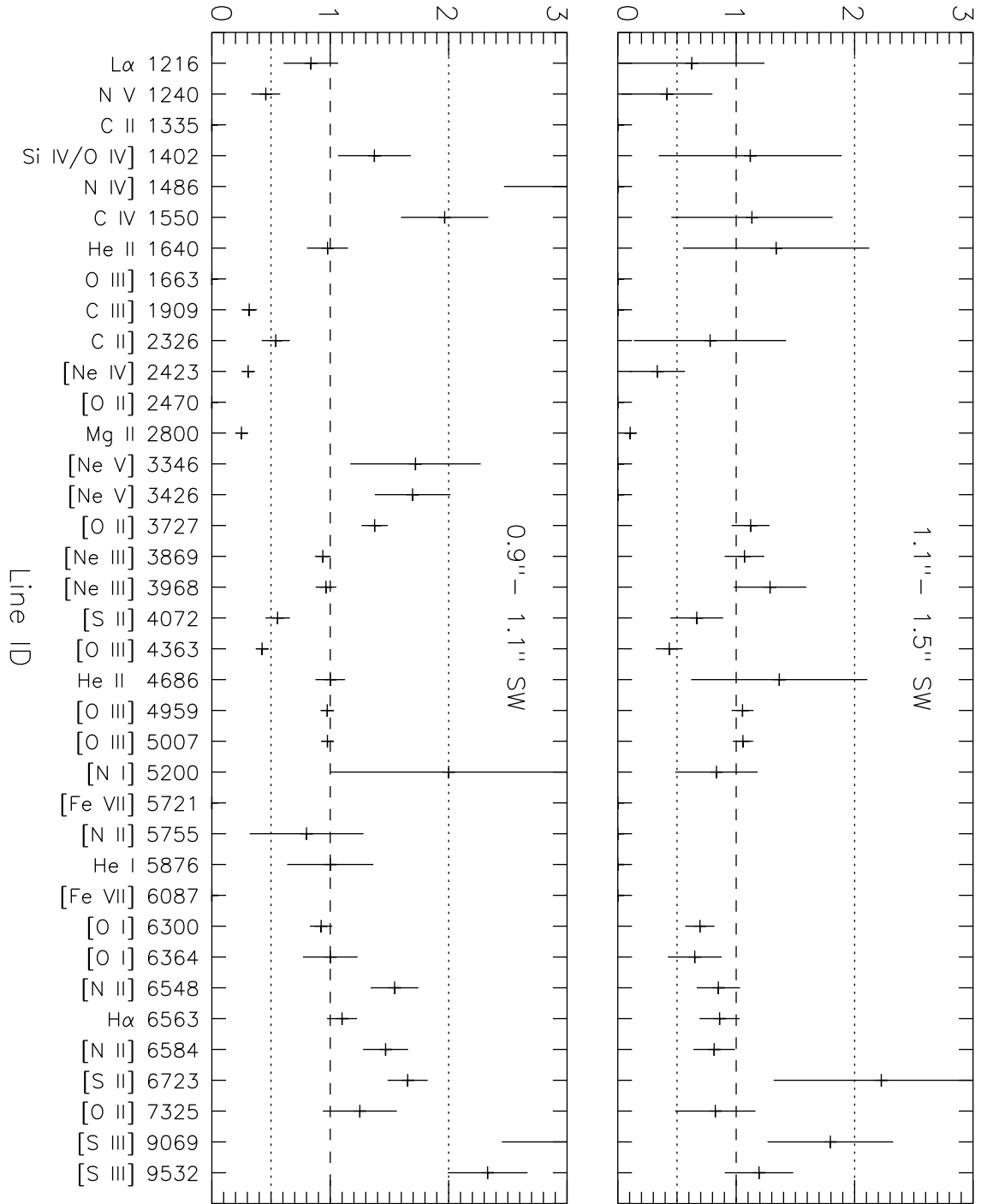




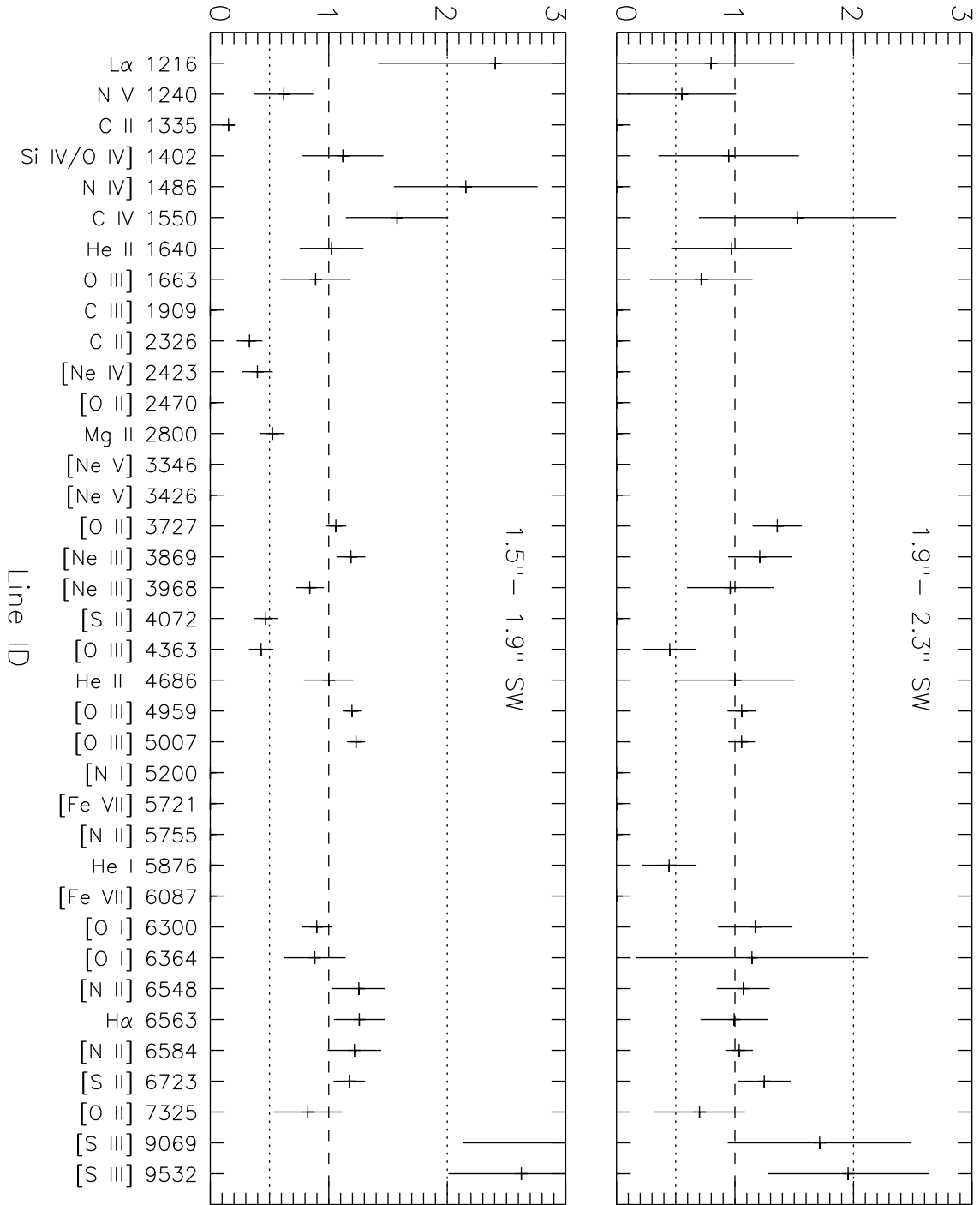
Model Ratio/Dereddened Ratio



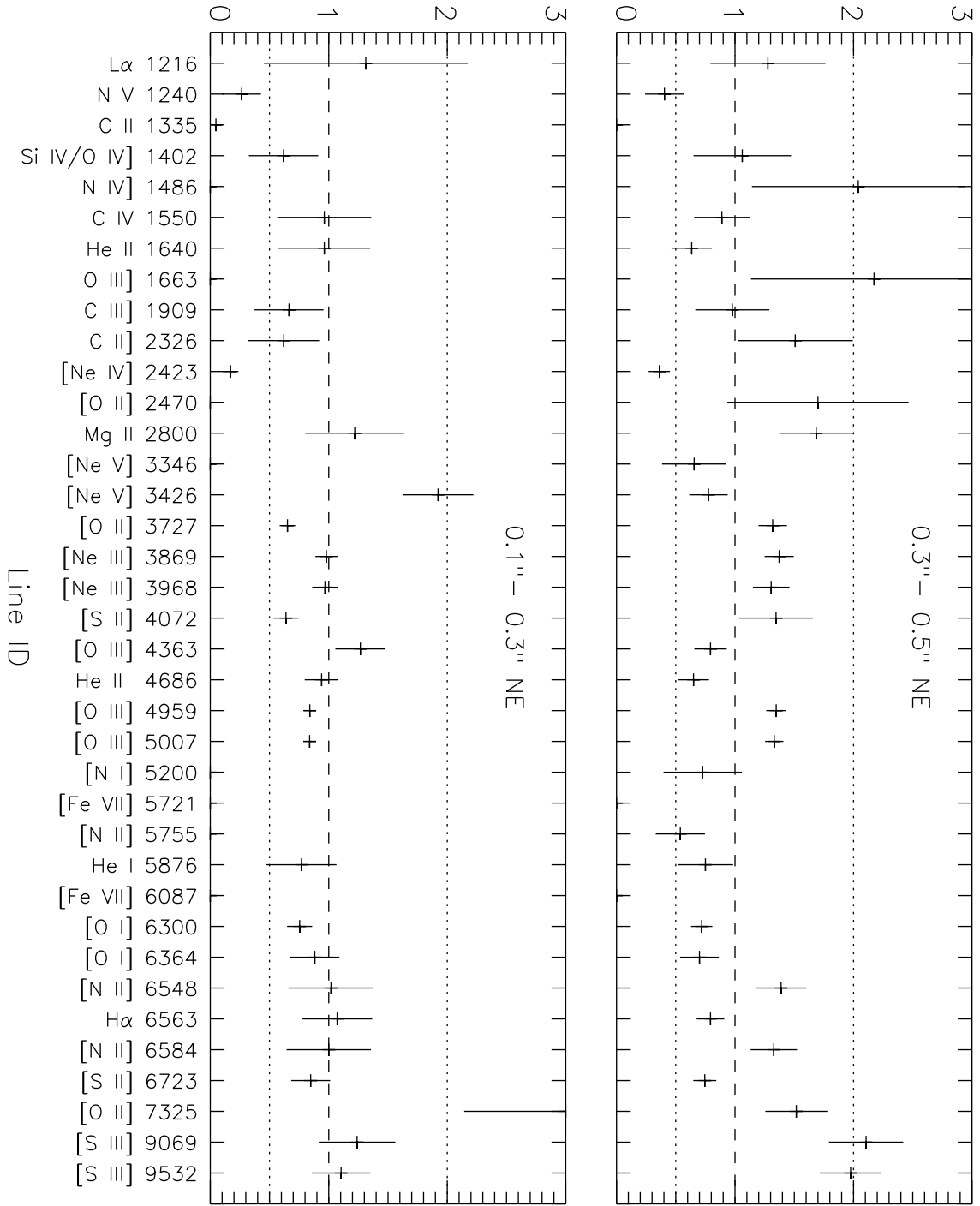
Model Ratio/Dereddened Ratio



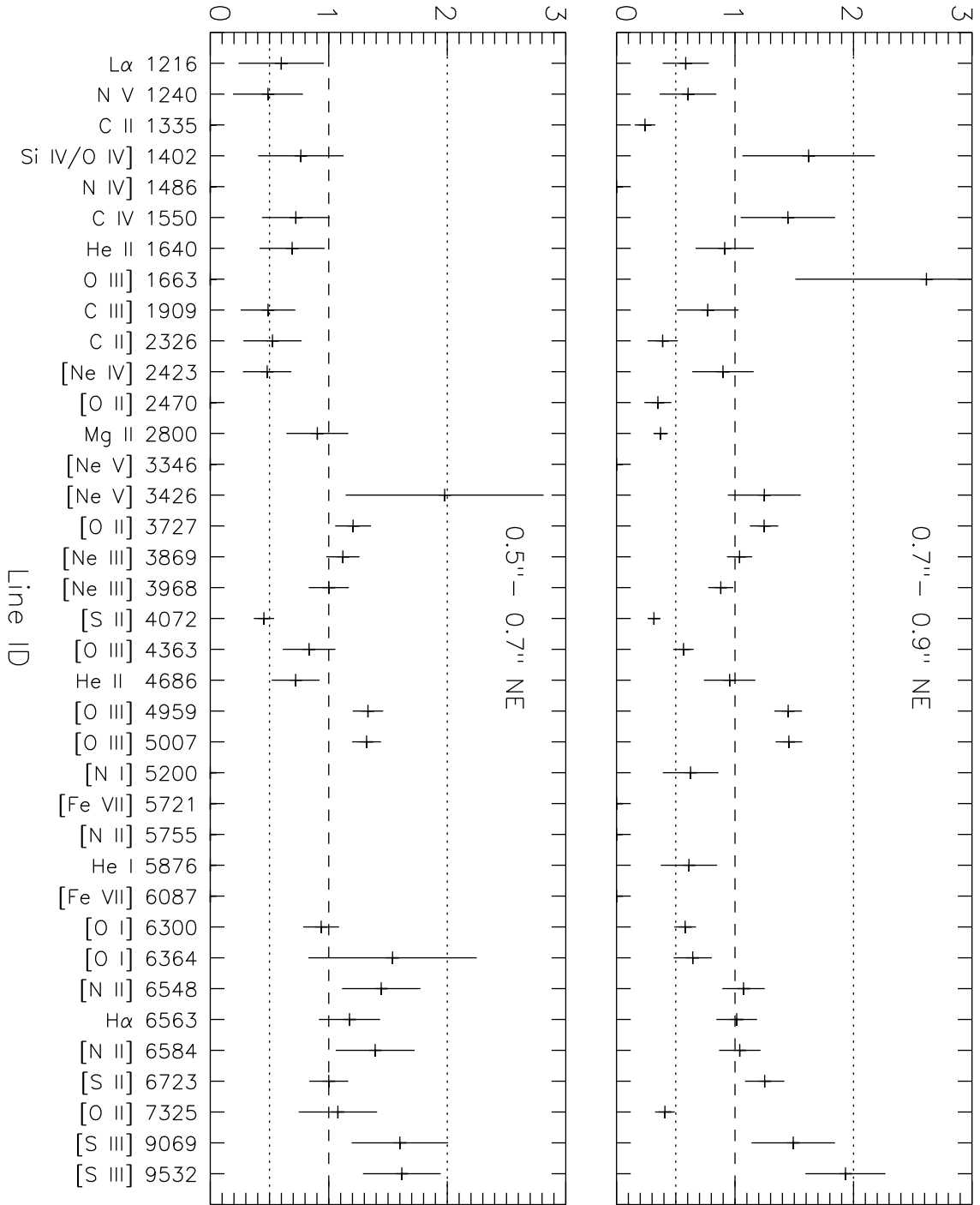
Model Ratio/Dereddened Ratio



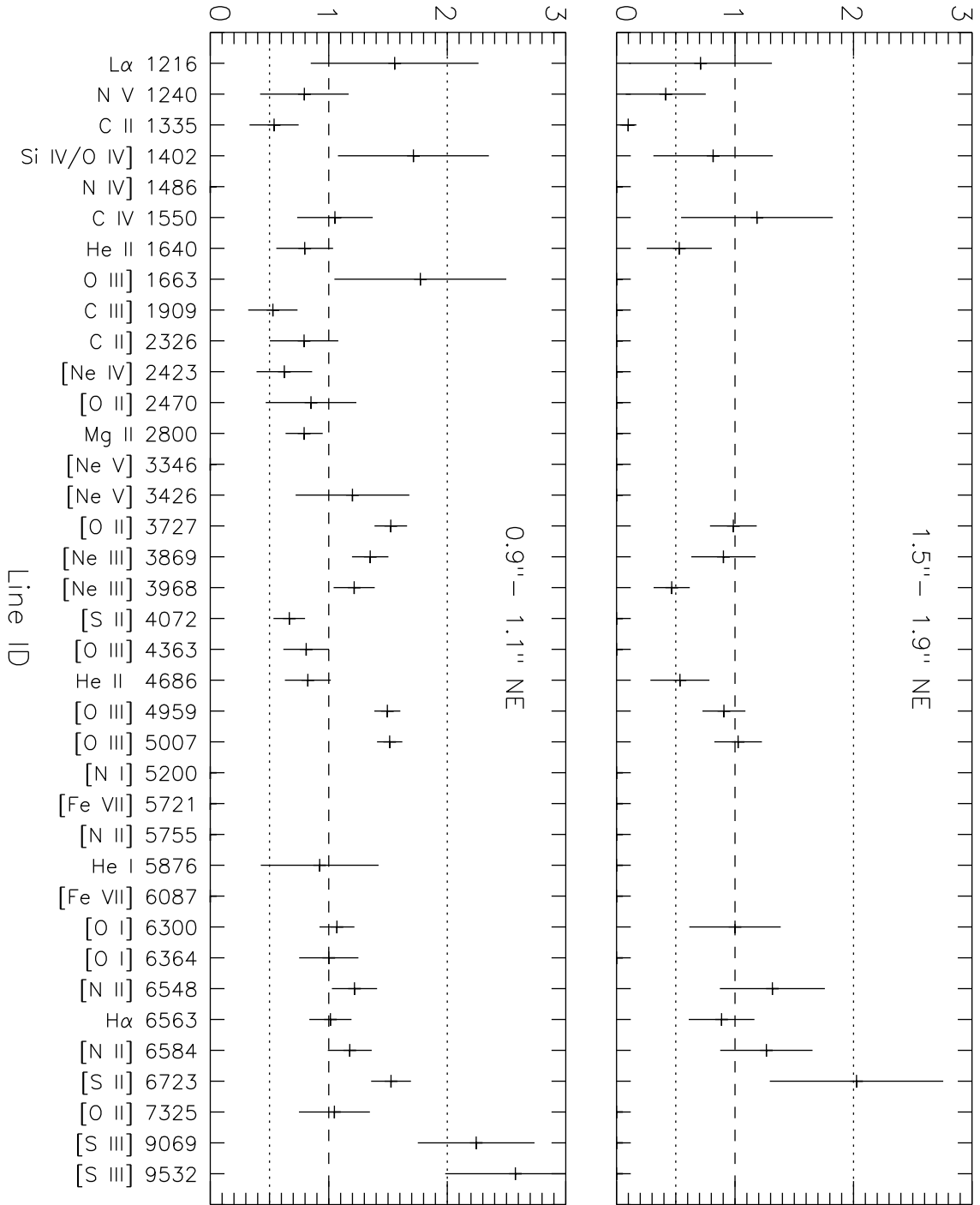
Model Ratio/Dereddened Ratio



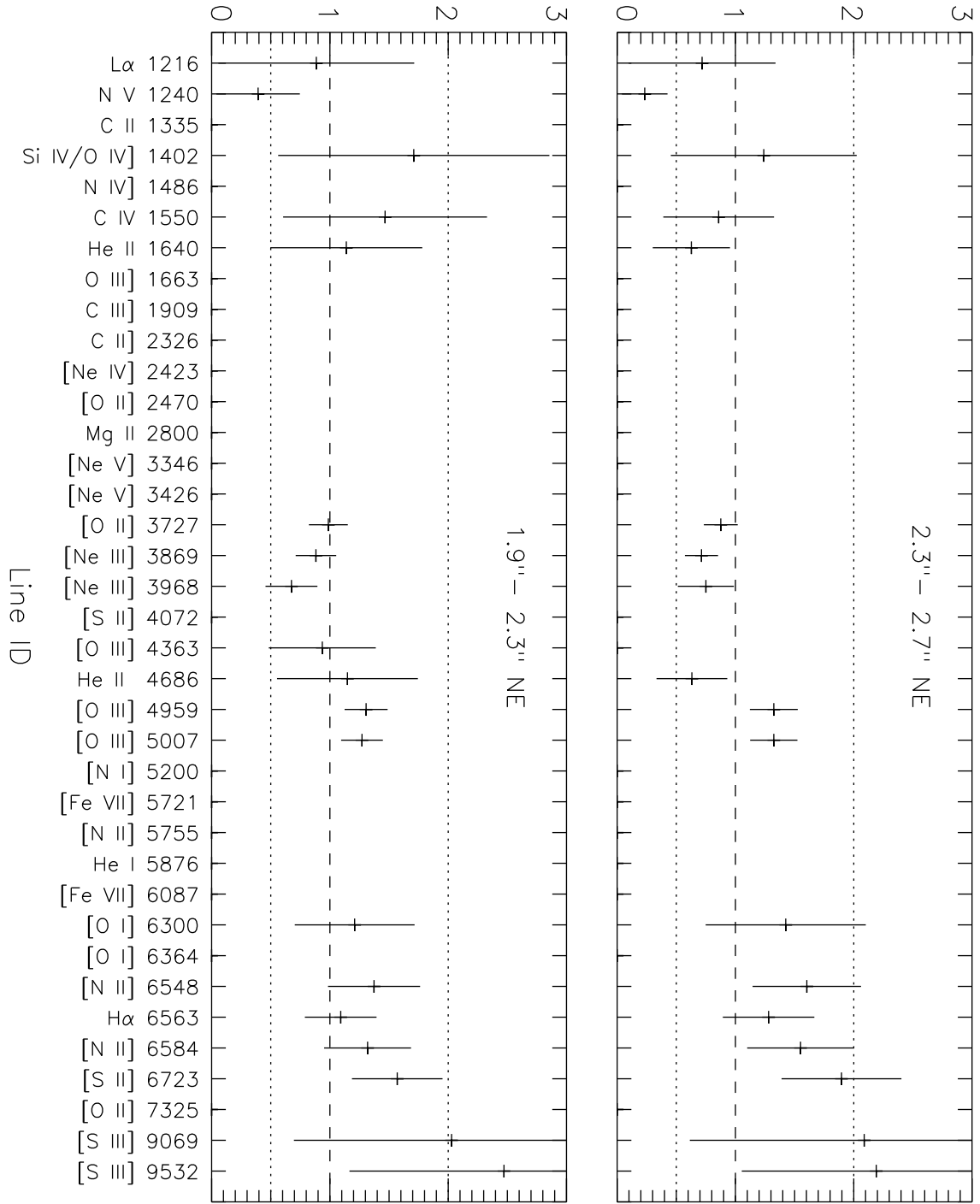
Model Ratio/Dereddened Ratio



Model Ratio/Dereddened Ratio



Model Ratio/Dereddened Ratio



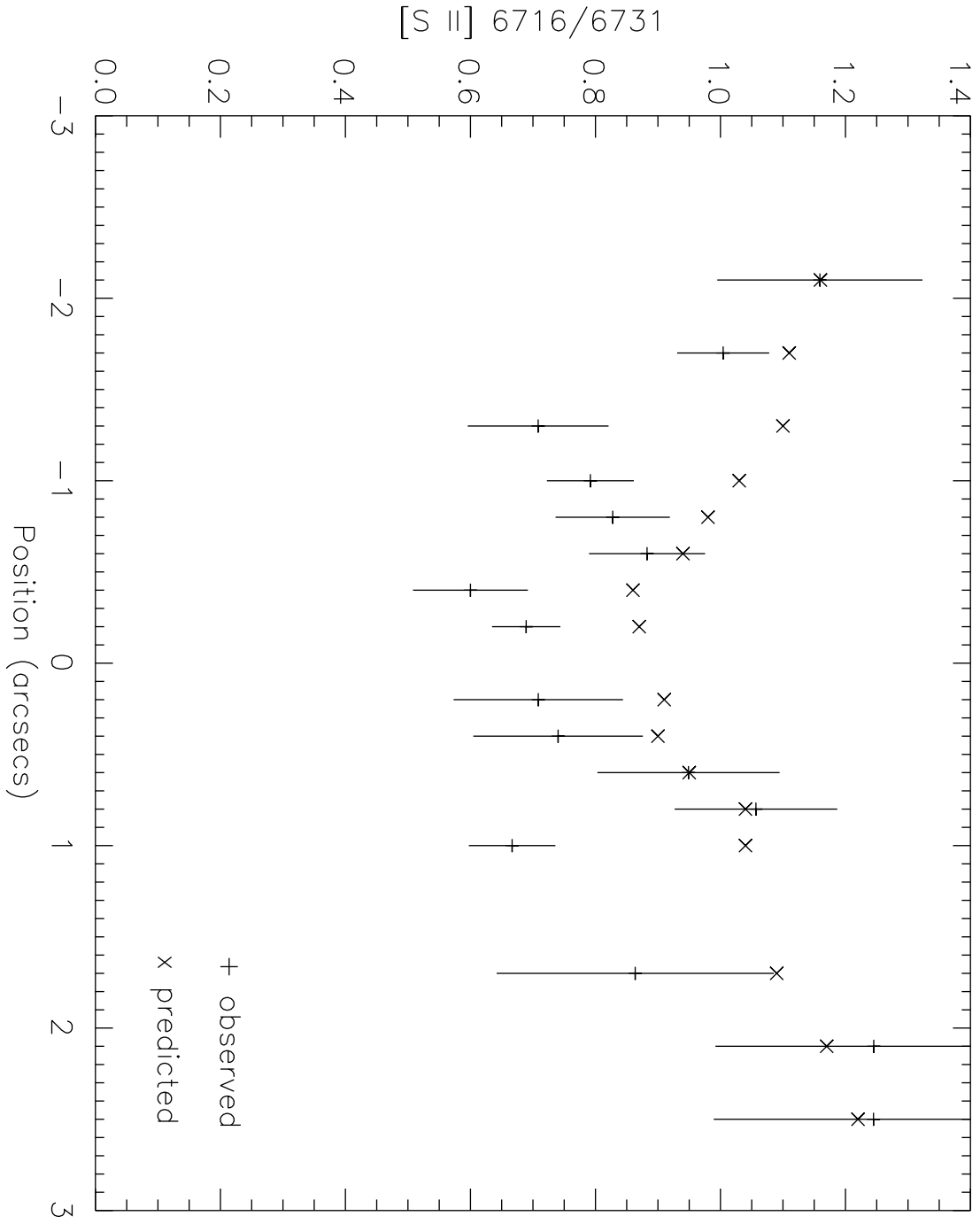




TABLE 1  
DEREDDENED NARROW-LINE RATIOS<sup>a</sup> AS A FUNCTION OF PROJECTED POSITION FOR PA = 221, SOUTHWEST

	0".1 – 0".3	0".3 – 0".5 (knot 26)	0".5 – 0".7 (knot 23)	0".7 – 0".9	0".9 – 1".1 (knot 22)	1".1 – 1".5	1".5 – 1".9 (knot 21)
Ly $\alpha$ $\lambda$ 1216	10.26 ( 3.03)	15.27 ( 6.99)	7.45 ( 3.05)	12.76 ( 6.42)	2.94 ( 0.81)	2.16 ( 2.12)	7.79 ( 3.03)
N V $\lambda$ 1240	2.12 ( 0.59)	3.21 ( 1.39)	1.60 ( 0.63)	3.09 ( 1.46)	0.90 ( 0.24)	0.53 ( 0.49)	1.45 ( 0.59)
C II $\lambda$ 1334	0.36 ( 0.10)	—	0.25 ( 0.09)	—	0.12 ( 0.03)	0.10 ( 0.08)	0.39 ( 0.10)
Si IV, O IV] $\lambda$ 1402	1.59 ( 0.37)	1.79 ( 0.60)	0.94 ( 0.29)	1.03 ( 0.38)	0.67 ( 0.15)	0.42 ( 0.29)	0.92 ( 0.37)
N IV] $\lambda$ 1486	—	—	0.23 ( 0.09)	0.47 ( 0.17)	0.21 ( 0.05)	—	0.32 ( 0.09)
C IV $\lambda$ 1550	9.92 ( 1.94)	7.32 ( 2.17)	5.97 ( 1.59)	6.68 ( 2.15)	2.08 ( 0.39)	1.88 ( 1.13)	4.20 ( 1.94)
He II $\lambda$ 1640	2.23 ( 0.45)	2.49 ( 0.73)	1.72 ( 0.46)	1.79 ( 0.56)	1.75 ( 0.31)	0.80 ( 0.47)	1.71 ( 0.45)
O III] $\lambda$ 1663	0.47 ( 0.14)	—	—	—	—	—	0.27 ( 0.14)
C III], Si III] $\lambda$ 1909	4.07 ( 0.90)	8.43 ( 2.66)	2.49 ( 0.79)	7.18 ( 2.51)	4.56 ( 0.94)	—	—
C II], [O III] $\lambda$ 2326	0.57 ( 0.15)	2.30 ( 0.79)	1.22 ( 0.38)	2.89 ( 1.08)	1.00 ( 0.22)	0.68 ( 0.56)	1.63 ( 0.15)
[Ne IV] $\lambda$ 2423	1.77 ( 0.33)	1.68 ( 0.48)	1.11 ( 0.30)	1.92 ( 0.60)	1.24 ( 0.22)	0.57 ( 0.40)	0.83 ( 0.33)
[O II] $\lambda$ 2470	0.51 ( 0.12)	0.39 ( 0.12)	—	—	—	—	—
Mg II $\lambda$ 2800	1.20 ( 0.28)	1.12 ( 0.21)	0.95 ( 0.17)	1.39 ( 0.26)	0.32 ( 0.06)	0.86 ( 0.33)	1.18 ( 0.28)
O III $\lambda$ 3133	0.76 ( 0.16)	0.67 ( 0.21)	—	—	—	—	—
[Ne V] $\lambda$ 3346	0.41 ( 0.07)	0.33 ( 0.11)	0.35 ( 0.14)	0.38 ( 0.13)	0.25 ( 0.08)	—	—
[Ne V] $\lambda$ 3426	1.14 ( 0.10)	0.93 ( 0.16)	1.19 ( 0.17)	0.91 ( 0.16)	0.69 ( 0.13)	—	—
[Fe VII] $\lambda$ 3588	0.16 ( 0.06)	—	—	—	—	—	—
[O II] $\lambda$ 3727	1.43 ( 0.14)	2.31 ( 0.28)	2.29 ( 0.20)	3.13 ( 0.24)	2.24 ( 0.18)	3.29 ( 0.47)	3.84 ( 0.14)
[Fe VII] $\lambda$ 3760	0.31 ( 0.06)	—	—	—	—	—	—
[Ne III] $\lambda$ 3869	1.81 ( 0.10)	1.76 ( 0.17)	1.44 ( 0.13)	1.36 ( 0.12)	1.27 ( 0.09)	1.15 ( 0.18)	1.07 ( 0.10)
H $\delta$ , He I $\lambda$ 3889	0.38 ( 0.05)	0.34 ( 0.06)	0.21 ( 0.06)	0.16 ( 0.05)	0.19 ( 0.04)	0.20 ( 0.09)	0.21 ( 0.05)
[Ne III] $\lambda$ 3967, He $\epsilon$	0.70 ( 0.05)	0.65 ( 0.11)	0.58 ( 0.07)	0.55 ( 0.07)	0.55 ( 0.05)	0.42 ( 0.10)	0.56 ( 0.05)
[S II] $\lambda$ 4072	0.41 ( 0.05)	0.34 ( 0.07)	0.25 ( 0.05)	0.34 ( 0.05)	0.27 ( 0.05)	0.21 ( 0.07)	0.32 ( 0.05)
H $\delta\lambda$ 4100	0.46 ( 0.05)	0.38 ( 0.06)	0.34 ( 0.08)	0.31 ( 0.06)	0.42 ( 0.05)	0.23 ( 0.08)	0.34 ( 0.05)
H $\gamma$ $\lambda$ 4340	0.67 ( 0.05)	0.46 ( 0.06)	0.63 ( 0.07)	0.50 ( 0.05)	0.53 ( 0.04)	0.63 ( 0.12)	0.50 ( 0.05)
[O III] $\lambda$ 4363	0.35 ( 0.05)	0.24 ( 0.05)	0.31 ( 0.05)	0.18 ( 0.04)	0.33 ( 0.04)	0.23 ( 0.06)	0.21 ( 0.05)
He II $\lambda$ 4686	0.31 ( 0.04)	0.35 ( 0.06)	0.24 ( 0.04)	0.25 ( 0.04)	0.24 ( 0.03)	0.11 ( 0.06)	0.24 ( 0.04)
H $\beta$	1.00 ( 0.00)	1.00 ( 0.00)	1.00 ( 0.00)	1.00 ( 0.00)	1.00 ( 0.00)	1.00 ( 0.00)	1.00 ( 0.00)
[O III] $\lambda$ 4959	5.34 ( 0.30)	4.53 ( 0.37)	4.17 ( 0.25)	3.48 ( 0.20)	4.32 ( 0.25)	3.76 ( 0.33)	2.61 ( 0.30)
[O III] $\lambda$ 5007	15.87 ( 0.65)	13.61 ( 1.09)	12.71 ( 0.83)	10.81 ( 0.58)	12.95 ( 0.71)	11.24 ( 0.91)	7.61 ( 0.65)
[N I] $\lambda$ 5200	—	—	0.09 ( 0.04)	0.09 ( 0.03)	0.04 ( 0.02)	0.12 ( 0.05)	—
[Fe VII] $\lambda$ 5721	0.13 ( 0.03)	—	—	—	—	—	—
[N II] $\lambda$ 5755	—	—	—	—	0.05 ( 0.03)	—	—
He I $\lambda$ 5876	0.22 ( 0.05)	0.12 ( 0.06)	0.13 ( 0.05)	0.10 ( 0.06)	0.11 ( 0.04)	—	—

TABLE 1—*Continued*

	0''.1 – 0''.3	0''.3 – 0''.5 (knot 26)	0''.5 – 0''.7 (knot 23)	0''.7 – 0''.9	0''.9 – 1''.1 (knot 22)	1''.1 – 1''.5	1''.5 – 1''.9 (knot 25)	1''.9 – (knot
[Fe VII] $\lambda$ 6087	0.33 ( 0.05)	0.09 ( 0.07)	0.11 ( 0.05)	—	—	—	—	—
[O I] $\lambda$ 6300	0.86 ( 0.07)	0.72 ( 0.10)	0.80 ( 0.11)	0.51 ( 0.07)	0.36 ( 0.04)	0.62 ( 0.11)	0.49 ( 0.07)	0.41 (
[O I] $\lambda$ 6364	0.42 ( 0.05)	0.12 ( 0.04)	0.19 ( 0.05)	0.10 ( 0.04)	0.13 ( 0.03)	0.20 ( 0.07)	0.17 ( 0.05)	0.14 (
[N II] $\lambda$ 6548	0.72 ( 0.27)	0.79 ( 0.15)	0.61 ( 0.10)	0.52 ( 0.16)	0.46 ( 0.06)	0.93 ( 0.20)	0.67 ( 0.12)	0.86 (
H $\alpha$ $\lambda$ 6563	3.60 ( 0.83)	2.55 ( 0.54)	2.53 ( 0.40)	2.20 ( 0.60)	2.61 ( 0.30)	3.35 ( 0.66)	2.29 ( 0.39)	2.90 (
[N II] $\lambda$ 6584	2.16 ( 0.82)	2.37 ( 0.44)	1.83 ( 0.31)	1.56 ( 0.47)	1.39 ( 0.18)	2.79 ( 0.60)	1.99 ( 0.37)	2.58 (
[S II] $\lambda$ 6716	0.41 ( 0.04)	0.27 ( 0.05)	0.52 ( 0.07)	0.49 ( 0.08)	0.35 ( 0.04)	0.71 ( 0.13)	0.75 ( 0.09)	0.86 (
[S II] $\lambda$ 6731	0.60 ( 0.05)	0.45 ( 0.09)	0.59 ( 0.08)	0.59 ( 0.09)	0.44 ( 0.05)	1.00 ( 0.19)	0.75 ( 0.09)	0.74 (
[Ar III] $\lambda$ 7136	0.18 ( 0.04)	0.23 ( 0.08)	0.21 ( 0.06)	0.23 ( 0.06)	0.20 ( 0.04)	0.20 ( 0.06)	0.14 ( 0.05)	0.18 (
[O II] $\lambda$ 7325	0.27 ( 0.04)	0.18 ( 0.06)	0.19 ( 0.05)	0.13 ( 0.05)	0.12 ( 0.03)	0.17 ( 0.07)	0.17 ( 0.06)	0.20 (
[S III] $\lambda$ 9069	0.72 ( 0.22)	0.26 ( 0.08)	0.36 ( 0.08)	0.26 ( 0.08)	0.23 ( 0.05)	0.44 ( 0.13)	0.18 ( 0.08)	0.42 (
[S III] $\lambda$ 9532	1.74 ( 0.37)	0.92 ( 0.18)	1.01 ( 0.19)	0.82 ( 0.17)	0.76 ( 0.11)	1.61 ( 0.39)	0.65 ( 0.15)	0.89 (
F (H $\beta$ ) <sup>b</sup>	9.76 (0.37)	4.31 (0.33)	3.65 (0.21)	2.35 (0.11)	4.52 (0.24)	1.90 (0.15)	2.35 (0.14)	1.07 (
E(B-V)	0.10 (0.04)	0.25 (0.06)	0.17 (0.06)	0.32 (0.07)	0.27 (0.04)	0.01 (0.12)	0.24 (0.06)	0.09 (

<sup>a</sup>Relative to H $\beta$ . Errors are given in parentheses.

<sup>b</sup>Flux of H $\beta$  ( $\times 10^{-15}$  ergs s $^{-1}$  cm $^{-2}$ ) in bin with 0''.1 width and specified length.

TABLE 2  
DEREDDENED NARROW-LINE RATIOS<sup>a</sup> AS A FUNCTION OF PROJECTED POSITION FOR PA = 221, NORTHEAST

	0".1 – 0".3	0".3 – 0".5 (knot 1)	0".5 – 0".7	0".7 – 0".9 (knot 10)	0".9 – 1".1 (knot 10)	1".5 – 1".9 (knot 4)	1".9 –
Ly $\alpha$ $\lambda$ 1216	21.73 (14.26)	7.24 ( 2.75)	27.16 (16.33)	22.67 ( 9.23)	10.99 ( 5.00)	28.36 (24.11)	20.27 (
N V $\lambda$ 1240	7.39 ( 4.54)	0.47 ( 0.19)	0.76 ( 0.46)	0.58 ( 0.23)	0.34 ( 0.16)	2.36 ( 1.92)	1.45 (
C II $\lambda$ 1334	1.47 ( 0.76)	—	—	0.25 ( 0.09)	0.13 ( 0.05)	0.61 ( 0.43)	—
Si IV, O IV] $\lambda$ 1402	2.83 ( 1.34)	0.49 ( 0.19)	1.23 ( 0.58)	0.58 ( 0.20)	0.35 ( 0.13)	1.73 ( 1.07)	0.79 (
N IV] $\lambda$ 1486	—	0.25 ( 0.11)	—	—	—	—	—
C IV $\lambda$ 1550	12.40 ( 5.11)	2.97 ( 0.78)	5.76 ( 2.28)	3.52 ( 0.97)	3.07 ( 0.93)	7.68 ( 4.15)	6.67 (
He II $\lambda$ 1640	2.38 ( 0.96)	1.45 ( 0.39)	1.81 ( 0.72)	1.60 ( 0.43)	1.23 ( 0.37)	3.08 ( 1.60)	1.95 (
O III] $\lambda$ 1663	—	0.23 ( 0.11)	—	0.26 ( 0.11)	0.22 ( 0.09)	—	—
C III], Si III] $\lambda$ 1909	5.27 ( 2.31)	2.19 ( 0.70)	4.31 ( 2.04)	2.52 ( 0.85)	3.20 ( 1.26)	—	—
C III], [O III] $\lambda$ 2326	1.87 ( 0.90)	0.59 ( 0.19)	1.41 ( 0.66)	1.80 ( 0.59)	0.96 ( 0.35)	—	—
[Ne IV] $\lambda$ 2423	1.40 ( 0.54)	0.72 ( 0.18)	0.75 ( 0.32)	0.59 ( 0.17)	0.40 ( 0.15)	—	—
[O II] $\lambda$ 2470	—	0.20 ( 0.09)	—	0.43 ( 0.14)	0.20 ( 0.09)	—	—
Mg II $\lambda$ 2800	1.05 ( 0.36)	0.54 ( 0.10)	0.83 ( 0.24)	1.91 ( 0.31)	1.01 ( 0.20)	—	—
O III $\lambda$ 3133	—	0.48 ( 0.17)	—	—	—	—	—
[Ne V] $\lambda$ 3346	—	0.29 ( 0.12)	—	—	—	—	—
[Ne V] $\lambda$ 3426	1.03 ( 0.16)	0.67 ( 0.14)	0.45 ( 0.19)	0.81 ( 0.20)	0.50 ( 0.20)	—	—
[Fe VII] $\lambda$ 3588	—	—	—	—	—	—	—
[O II] $\lambda$ 3727	1.98 ( 0.20)	1.76 ( 0.16)	2.39 ( 0.30)	3.02 ( 0.29)	2.77 ( 0.25)	5.70 ( 1.14)	4.56 (
[Fe VII] $\lambda$ 3760	0.30 ( 0.08)	—	—	—	—	—	—
[Ne III] $\lambda$ 3869	1.48 ( 0.14)	1.45 ( 0.13)	1.60 ( 0.20)	1.56 ( 0.16)	1.23 ( 0.14)	1.43 ( 0.43)	1.44 (
H $\delta$ , He I $\lambda$ 3889	0.20 ( 0.06)	0.27 ( 0.06)	0.37 ( 0.10)	0.23 ( 0.06)	0.20 ( 0.07)	—	—
[Ne III] $\lambda$ 3967, He $\epsilon$	0.63 ( 0.07)	0.59 ( 0.07)	0.71 ( 0.12)	0.75 ( 0.09)	0.56 ( 0.08)	1.16 ( 0.38)	0.80 (
[S II] $\lambda$ 4072	0.36 ( 0.06)	0.26 ( 0.06)	0.53 ( 0.10)	0.57 ( 0.08)	0.30 ( 0.06)	—	—
H $\delta\lambda$ 4100	0.27 ( 0.05)	0.27 ( 0.05)	0.35 ( 0.08)	0.42 ( 0.10)	0.24 ( 0.06)	—	0.40 (
H $\gamma$ $\lambda$ 4340	0.42 ( 0.06)	0.57 ( 0.06)	0.55 ( 0.09)	0.68 ( 0.08)	0.50 ( 0.06)	—	0.66 (
[O III] $\lambda$ 4363	0.30 ( 0.05)	0.29 ( 0.05)	0.30 ( 0.08)	0.46 ( 0.07)	0.21 ( 0.05)	—	0.31 (
He II $\lambda$ 4686	0.33 ( 0.05)	0.20 ( 0.04)	0.25 ( 0.07)	0.22 ( 0.05)	0.17 ( 0.04)	0.43 ( 0.20)	0.27 (
H $\beta$	1.00 ( 0.00)	1.00 ( 0.00)	1.00 ( 0.00)	1.00 ( 0.00)	1.00 ( 0.00)	1.00 ( 0.00)	1.00 (
[O III] $\lambda$ 4959	4.24 ( 0.27)	4.66 ( 0.29)	4.66 ( 0.45)	4.10 ( 0.33)	3.54 ( 0.26)	4.05 ( 0.81)	4.02 (
[O III] $\lambda$ 5007	12.74 ( 0.81)	14.14 ( 0.82)	14.10 ( 1.30)	12.26 ( 0.95)	10.49 ( 0.74)	10.74 ( 2.10)	12.39 (
[N I] $\lambda$ 5200	—	0.11 ( 0.05)	—	0.16 ( 0.06)	—	—	—
[Fe VII] $\lambda$ 5721	—	—	—	—	—	—	—
[N II] $\lambda$ 5755	—	0.13 ( 0.05)	—	—	—	—	—
He I $\lambda$ 5876	0.13 ( 0.05)	0.16 ( 0.05)	—	0.18 ( 0.07)	0.13 ( 0.07)	—	—

TABLE 2—*Continued*

	0".1 – 0".3	0".3 – 0".5 (knot 1)	0".5 – 0".7	0".7 – 0".9 (knot 10)	0".9 – 1".1 (knot 10)	1".5 – 1".9 (knot 4)	1".9 – 2".3 (knot 4)	2".3 – (knot 4)
[Fe VII] $\lambda$ 6087	—	—	—	—	—	—	—	—
[O I] $\lambda$ 6300	0.57 ( 0.08)	0.96 ( 0.12)	0.62 ( 0.10)	0.95 ( 0.15)	0.58 ( 0.08)	0.70 ( 0.27)	0.43 ( 0.18)	0.40 ( 0.15)
[O I] $\lambda$ 6364	0.17 ( 0.04)	0.30 ( 0.07)	0.13 ( 0.06)	0.28 ( 0.07)	0.20 ( 0.05)	—	—	—
[N II] $\lambda$ 6548	0.54 ( 0.19)	0.72 ( 0.11)	0.61 ( 0.14)	0.84 ( 0.14)	0.83 ( 0.13)	0.92 ( 0.31)	0.67 ( 0.19)	0.63 ( 0.23)
H $\alpha$ $\lambda$ 6563	2.68 ( 0.74)	3.67 ( 0.54)	2.46 ( 0.54)	2.84 ( 0.48)	2.85 ( 0.50)	3.26 ( 1.02)	2.63 ( 0.73)	2.25 ( 0.71)
[N II] $\lambda$ 6584	1.60 ( 0.57)	2.17 ( 0.32)	1.84 ( 0.44)	2.50 ( 0.42)	2.48 ( 0.39)	2.76 ( 0.85)	2.01 ( 0.56)	1.89 ( 0.61)
[S II] $\lambda$ 6716	0.30 ( 0.07)	0.61 ( 0.10)	0.62 ( 0.12)	0.66 ( 0.10)	0.47 ( 0.06)	0.55 ( 0.24)	0.68 ( 0.19)	0.65 ( 0.22)
[S II] $\lambda$ 6731	0.42 ( 0.10)	0.83 ( 0.13)	0.66 ( 0.12)	0.62 ( 0.09)	0.71 ( 0.09)	0.64 ( 0.27)	0.55 ( 0.16)	0.52 ( 0.18)
[Ar III] $\lambda$ 7136	0.13 ( 0.05)	0.25 ( 0.05)	0.24 ( 0.07)	0.36 ( 0.08)	0.13 ( 0.05)	0.37 ( 0.27)	0.22 ( 0.14)	—
[O II] $\lambda$ 7325	0.14 ( 0.04)	0.29 ( 0.05)	0.26 ( 0.08)	0.49 ( 0.10)	0.21 ( 0.06)	—	—	—
[S III] $\lambda$ 9069	0.46 ( 0.12)	0.47 ( 0.07)	0.55 ( 0.16)	0.55 ( 0.13)	0.41 ( 0.09)	—	0.35 ( 0.23)	0.34 ( 0.21)
[S III] $\lambda$ 9532	1.25 ( 0.28)	1.22 ( 0.16)	1.33 ( 0.34)	1.03 ( 0.18)	0.87 ( 0.20)	—	0.70 ( 0.37)	0.79 ( 0.31)
F (H $\beta$ ) <sup>b</sup>	6.18 (0.37)	5.07 (0.29)	1.78 (0.16)	3.21 (0.24)	3.31 (0.21)	0.53 (0.10)	0.76 (0.10)	0.69 (0.10)
E(B-V)	0.36 (0.09)	0.03 (0.06)	0.14 (0.08)	0.12 (0.06)	0.06 (0.06)	0.22 (0.11)	0.21 (0.11)	0.27 (0.11)

<sup>a</sup>Relative to H $\beta$ . Errors are given in parentheses.

<sup>b</sup>Flux of H $\beta$  ( $\times 10^{-15}$  ergs s<sup>-1</sup> cm<sup>-2</sup>) in bin with 0".1 width and specified length.